Article

Hydrodynamics of Moonpool-Type Floaters: A Theoretical and a CFD Formulation

Anargyros S. Mavrakos [1], **Dimitrios N. Konispoliatis** [1,*], **Dimitrios G. Ntouras** [2], **George P. Papadakis** [2] **and Spyros A. Mavrakos** [1]

[1] Laboratory for Floating Structures and Mooring Systems, School of Naval Architecture and Marine Engineering, National Technical University of Athens, GR 157-73 Athens, Greece; rgmavrakos@gmail.com (A.S.M.); mavrakos@naval.ntua.gr (S.A.M.)

[2] Laboratory for Naval and Marine Hydrodynamics, School of Naval Architecture and Marine Engineering, National Technical University of Athens, GR 157-73 Athens, Greece; ntourasd@fluid.mech.ntua.gr (D.G.N.); papis@fluid.mech.ntua.gr (G.P.P.)

* Correspondence: dkonisp@naval.ntua.gr; Tel.: +30-210-772-1790

Abstract: Moonpool-type floaters were initially proposed for applications such as artificial islands or as protecting barriers around a small area enabling work at the inner surface to be carried out in relatively calm water. In recent years, a growing interest on such structures has been noted, especially in relation to their use as heaving wave energy converters or as oscillating water column (OWC) devices for the extraction of energy from waves. Furthermore, in the offshore marine industry, several types of vessels are frequently constructed with moonpools. The present paper deals with the hydrodynamics of bottomless cylindrical bodies having vertical symmetry axis and floating in a water of finite depth. Two computation methods were implemented and compared: a theoretical approach solving analytically the corresponding diffraction problem around the moonpool floater and a computational fluid dynamics (CFD) solver, which considers the viscous effects near the sharp edges of the body (vortex shedding) as non-negligible. Two different moonpool-type configurations were examined, and some interesting phenomena were discussed concerning the viscous effects and irregularities caused by the resonance of the confined fluid.

Keywords: moonpool type floaters; viscous effects; computational fluid dynamics; theoretical formulation

1. Introduction

Moonpool-type floaters were initially proposed to be applied either as artificial islands or as structures enabling activities in their inner area, as they used their solid boundaries as protecting walls to the wave action. Nevertheless, in recent years, they have been associated with their use as wave energy converter (WEC) devices suitable for wave energy absorption, as well as floating pontoons for semi-submersible designs.

Several types of bottomless cylindrical hulls (known as moonpools) have been examined in the literature. The most common is a vertical cylinder with a vertical opening from the deck to keel through the hull [1], whereas square floaters with square moonpools have been also studied [2,3]. Additional types concern toroidal configurations consisting of a circular (core) section centered upon a large circle (ring) with an infinitesimally small [4] and finite [5] slenderness core-to-ring-radius ratio, as well as two coaxial surface piercing truncated circular cylinders [6]. The latter geometry was encompassed by an exterior partially immersed toroidal structure of finite volume and an interior coaxial free surface-piercing truncated cylinder. Thus, an internal annular free surface was developed, which was totally enclosed between the solid boundaries of the cylinders and open to the exterior fluid domain beneath the concentric bodies.

Hydrodynamics of the isolated truncated hollow cylindrical bodies have been investigated in the past. Garrett [7] presented an analytical solution of the wave scattering problem

by a vertical bottomless partially immersed circular cylinder with infinitesimal wall thickness using matched axisymmetric eigenfunction expansions. Analytical computations of the exciting wave forces and moments on the hollow cylindrical shell structure, together with sway and pitch hydrodynamic coefficients, were derived by Miloh [8]. He also derived analytic expressions for the amplification ratios of heave (pumping) and pitch (seiche) modes of water motions inside the pond. The corresponding hydrodynamic characteristics of an open-ended vertically floating circular cylinder, as well as the induced water motion in the interior basin, accounting for the effect of the finite wall thickness, were presented by [1,9]. Furthermore, Liu et al. [10] investigated the second-order sum frequency wave loads on a hollow cylindrical shell structure in long crested irregular seas. Additionally, in [11,12] the solutions of the diffraction and radiation problems of a moonpool cylindrical body of infinite thickness and of a partially bottom-opened moonpool were presented. A moonpool with a restricted entrance was also studied. In [13], it was shown that the motion of the water inside the body was amplified as the size of the moonpool entrance was reduced. In addition, Liu et al. [14] measured the viscous effect of a moonpool cylindrical structure with a restricted entrance by introducing a quadratic dissipation assuming an additional dissipative disk at the moonpool entrance.

Regarding the two coaxial surface piercing truncated circular cylinder configuration, the solutions of the linearized diffraction and radiation problems around two independently moving concentric truncated cylinders were presented in [6,15]. Furthermore, the mean- and the time-dependent second-order wave loads on such a type of floating structures were evaluated in [16,17]. Recently, Chao and Kim [18] investigated the hydrodynamic performance of a two-body WEC by applying analytical solutions, whereas Kong et al. [19] examined a moonpool platform-wave energy buoy composed of an inner cylindrical buoy and an outer toroidal-cylinder for wave power extraction by the relative heave motions between the inner and outer buoys.

Apart from wave energy applications, concentric surface-piecing circular cylindrical bodies have also been investigated, combined with the trapped wave modes that they can develop, i.e., the localized oscillations of the enclosed formed free surface area, whereas the motion in the exterior fluid region decayed to zero. Abramson [20] presented a comprehensive review of liquid sloshing problems in moving containers, while Shipway and Evans [21] examined the wave trapping phenomena by two concentric circular cylindrical shells with a vertical axis and a zero thickness. As an extension of [21]'s work, McIver and Newman [22] studied the case of vertically axisymmetric trapping structures, of finite volumes, composed by two concentric interior free surfaces.

All the aforementioned research is based on potential flow methodologies concerning the hydrodynamic solutions of several types of bottomless cylindrical hulls. Nevertheless, over the last decade, there has been a significant interest in computational fluid dynamics (CFD) modelling due to its detailed results. CFD modelling solves the fluid flow problem using Navier–Stokes equations, where the hydrodynamics of random-shape floating structures can be calculated in detail, providing representative results of the flow physics. Several authors have studied the importance of including viscosity in moonpool problems using CFD modelling. Lu et al. [23] investigated the possibility of finding an artificial, empirically-based damping coefficient to the free surface condition inside a moonpool device applied to potential flow models. The latter exhibit overestimated magnitudes of wave forces as the fluid resonance takes place; hence, by introducing an artificial damping term, the potential flow model may work as well as the viscous fluid model. Lu et al. [24] extended the results from [23] on the wave elevation inside a moonpool body; whereas, in [25,26], the piston-mode in a 2D moonpool under forced heave oscillations was evaluated using a linear potential solver coupled to a viscous Navier–Stokes modelling. In addition, Fredriksen et al. [27] investigated, numerically and experimentally, how a low forward/incoming current speed influences the resonant piston-mode resonance in a moonpool. They concluded that the moonpool behavior was marginally reduced with a low forward velocity, whereas this reduction was dependent on the heave forcing amplitude.

Recently, in [28] a viscous damping model for energy losses of a 2D fluid response in a moonpool due to wall friction and flow separation was proposed. Furthermore, the limitations of boundary element method solvers when viscous effects near floater's sharp edges were taken into account and were exploited in [29] in the case of a moonpool type floater.

In the present article, two different geometric configurations of a moonpool-type floater were investigated; a floater encompassed by two coaxial, free-surface piercing toroidal cylinders with vertical symmetry axes (Configuration 1, see Figure 1a) and a floater consisting of an external toroidal cylinder and an internal coaxial surface piercing truncated circular cylinder (Configuration 2, see Figure 1b). In the annular and the cylindrical fluid areas formed between the cylinders' vertical walls, oscillations of the enclosed water columns were developed. A semi-analytical model was used to solve the wave diffraction problem in the context of linear potential theory [30]. The method of matched axisymmetric eigenfunction expansions was applied to solve the relevant hydrodynamic problem, according to which the flow field around and inside the examined body was subdivided in coaxial ring-shaped fluid regions. Hence, appropriate series representations of the velocity potential can be established in each region, which were matched at the boundaries of adjacent fluid domains by enforcing the continuity conditions of the hydrodynamic pressure and the radial velocity in order to determine the unknown coefficients in the expressions of the diffraction potential. The exciting wave forces/moments and the wave elevation on both case studies were calculated and compared focusing on the resonant wave frequencies. Furthermore, the accuracy of the semi-analytical formulation was assessed in comparison to high fidelity CFD simulations.
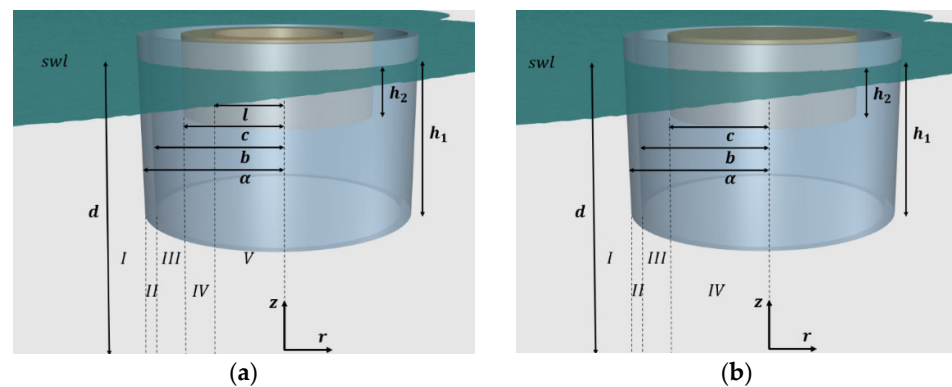
Figure 1. Two examined moonpool case studies exposed to the action of regular wave trains. Definitions and discretization of the flow field around the bodies: (**a**) two coaxial surface piercing moonpool vertical toroidal cylinders; (**b**) moonpool with a coaxial surface piercing truncated circular cylinder.

The present work is structured as follows: in Section 2 the solution of the diffraction problem is formulated, along with the evaluation of the hydrodynamic forces and wave elevation around/inside the examined case studies. Section 3 is dedicated to the presentation of the used CFD solver, whereas, in Section 4, the outcomes of the two methods (i.e., semi-analytical and CFD solvers) are compared for the two moonpool arrangements. Finally, conclusions are drawn in Section 5.

2. Material and Methods

2.1. Velocity Potential Representation

Two coaxial, free-surface piercing toroidal cylinders with vertical symmetry axes are considered floating in constant water depth d. The cylinders are exposed to the action of a regular wave-train of wave frequency ω and amplitude $H/2$. The draughts of the moonpool bodies are denoted by h_1 and h_2, respectively. Cylindrical co-ordinates (r, θ, z) are introduced with the z axis positive upwards and with origin on the seabed (see Figure 1). In the present formulation, viscous effects were neglected, whereas the fluid was assumed

incompressible. Furthermore, the fluid's motions were assumed to be small, so that the linearized diffracted problem could be considered.

The fluid flow is described by the velocity potential expressed as:

$$\Phi(r, \theta, z; t) = Re\left[\varphi(r, \theta, z)e^{-i\omega t}\right] \tag{1}$$

with

$$\varphi(r, \theta, z) = \varphi_D(r, \theta, z) = \varphi_0(r, \theta, z) + \varphi_7(r, \theta, z) \tag{2}$$

Here, φ_0 is the velocity potential of the undisturbed incident harmonic wave and φ_7 is the diffraction potential for the restrained body in the wave impact. The diffraction potential is described by the velocity potential φ_D.

The undisturbed velocity potential of an incident wave train propagating along the positive axis can be expressed in cylindrical coordinates as:

$$\varphi_0(r, \theta, z) = -i\omega \frac{H}{2} \frac{Z_0(z)}{Z_0'(d)} \sum_{m=0}^{\infty} \varepsilon_m i^m J_m(kr)\cos(m\theta) \tag{3}$$

In Equation (3) J_m stands for the mth order Bessel function of first kind, ε_m is the Neumann's symbol, i.e., $\varepsilon_0 = 1$, $\varepsilon_m = 2$ for $m \geq 1$, and Z_0 is derived by:

$$Z_0(z) = \left[\frac{1}{2}\left[1 + \frac{\sin h(2kd)}{2kd}\right]\right]^{-\frac{1}{2}} \cos h(kz) \tag{4}$$

with $Z_0'(d)$ being its derivative at $z = d$. The wave number k and the wave frequency ω are related by the dispersion equation i.e.,: $\omega^2 = kg\tan h(kd)$.

In accordance with Equation (3) the total diffracted potential of the flow field around the examined moonpool can be written in the form:

$$\varphi_D(r, \theta, z) = -i\omega \frac{H}{2} \sum_{m=0}^{\infty} \varepsilon_m i^m \Psi_{D,m}(r, z)\cos(m\theta) \tag{5}$$

The $\Psi_{D,m}$ denote the principal unknowns of the problem. The subscript D stands for the diffraction problem, whereas the subscript m indicates the modes that should be taken into consideration within the solution of the corresponding problem.

The potential φ_D must satisfy:

$$\Delta\varphi_D = \frac{\partial^2 \varphi_D}{\partial r^2} + \frac{1}{r}\frac{\partial \varphi_D}{\partial r} + \frac{1}{r^2}\frac{\partial^2 \varphi_D}{\partial \theta^2} + \frac{\partial^2 \varphi_D}{\partial z^2} = 0 \tag{6}$$

with the linearized boundary conditions:
on the free surface $z = d$:

$$\omega^2 \varphi_D - g\frac{\partial \varphi_D}{\partial z} = 0 \tag{7}$$

on the seabed $z = 0$:

$$\frac{\partial \varphi_D}{\partial z} = 0 \tag{8}$$

on the body's bottom ($z = d - h_1$, $b \leq r \leq a$ and $z = d - h_2$, $l \leq r \leq c$):

$$\frac{\partial \varphi_D}{\partial z} = 0 \tag{9}$$

on the body's side walls ($d - h_1 \leq z \leq d$, $r = a, b$ and $d - h_2 \leq z \leq d$, $r = c, l$):

$$\frac{\partial \varphi_D}{\partial r} = 0 \tag{10}$$

It is also required that the scattered potential satisfies an appropriate radiation condition as $r \to \infty$ which has the form [1,31]:

$$\lim_{r \to \infty} \sqrt{r} \left(\frac{\partial}{\partial r} - ik \right) \varphi_7 = 0 \tag{11}$$

In addition, both the velocity potential and its derivatives $\frac{\partial \varphi_D}{\partial r}$ must be continuous at the boundaries $r = a, b, c, l$ of the neighboring ring elements shown in Figure 1a. This results in:

for $0 < z < d - h_1$, and $r = a$:

$$\Psi^I_{D,m}(a, z) = \Psi^{II}_{D,m}(a, z) \tag{12}$$

$$\left. \frac{\partial \Psi^I_{D,m}(r,z)}{\partial r} \right|_{r=a} = \left. \frac{\partial \Psi^{II}_{D,m}(r,z)}{\partial r} \right|_{r=a} \tag{13}$$

for $0 < z < d - h_1$, and $r = b$:

$$\Psi^{II}_{D,m}(b, z) = \Psi^{III}_{D,m}(b, z) \tag{14}$$

$$\left. \frac{\partial \Psi^{II}_{D,m}(r,z)}{\partial r} \right|_{r=b} = \left. \frac{\partial \Psi^{III}_{D,m}(rz)}{\partial r} \right|_{r=b} \tag{15}$$

for $0 < z < d - h_2$, and $r = c$:

$$\Psi^{III}_{D,m}(c, z) = \Psi^{IV}_{D,m}(c, z) \tag{16}$$

$$\left. \frac{\partial \Psi^{III}_{D,m}(r,z)}{\partial r} \right|_{r=c} = \left. \frac{\partial \Psi^{IV}_{D,m}(r,z)}{\partial r} \right|_{r=c} \tag{17}$$

for $0 < z < d - h_2$, and $r = l$:

$$\Psi^{III}_{D,m}(c, z) = \Psi^{IV}_{D,m}(\mathbf{c}, z) \tag{18}$$

$$\left. \frac{\partial \Psi^{III}_{D,m}(r,z)}{\partial r} \right|_{r=c} = \left. \frac{\partial \Psi^{IV}_{D,m}(r,z)}{\partial r} \right|_{r=c} \tag{19}$$

The superscripts *I, II, III, IV, V* imply quantities corresponding to respective types of ring elements.

The procedure for the determination of the velocity potential around a moonpool body that is exposed to the action of surface gravity waves has been presented thoroughly in previous studies: [1,5,6,9,15], to name a few. This procedure is extended here to the case of two coaxial surface piercing toroidal vertical cylinders. The following equations present proper series representations of the functions $\Psi^i_{D,m}$, $i = I, II, III, IV, V$ in each fluid region around the body:

(a) Infinite fluid domain, Type I ($a \leq r$, $0 \leq z \leq d$):

$$\frac{1}{d} \Psi^I_{D,m} = \left\{ J_m(kr) - \frac{J_m(ka)}{H_m(ka)} H_m(kr) \right\} \frac{Z_0(z)}{dZ'_0(d)} + \sum_{j=0}^{\infty} F^I_{mj} \frac{K_m(a_j r)}{K_m(a_j a)} Z_j(z) \tag{20}$$

where H_m, K_m is the m-th order Hankel function of the first kind and the modified Bessel function of the second type, respectively. In addition, $Z_j(z)$ are orthonormal functions in $[0, d]$ defined by Equation (4) for $j = 0$ and for $j > 0$:

$$Z_j(z) = \left[\frac{1}{2} \left[1 + \frac{\sin(2a_j d)}{2a_j d} \right] \right]^{-\frac{1}{2}} \cos(a_j z), \ j > 0 \tag{21}$$

The terms a_j are the roots of the transcendental equation: $\omega^2 + a_j g \tan(a_j d) = 0$, which proposes one imaginary $a_0 = -ik$, $k > 0$ and infinite number of real roots.

(b)   Second fluid domain, Type II ($b \leq r \leq a$, $0 \leq z \leq d - h_1$):

$$\frac{1}{d}\Psi_{D,m}^{II} = \sum_{n=0}^{\infty} \varepsilon_n \left[R_{mn}^{II}(r)F_{mn}^{II} + R_{mn}^{*II}(r)F_{mn}^{*II} \right] \cos\left(\frac{n\pi z}{d - h_1}\right) \tag{22}$$

where ε_n stands for the Neumann's symbol and the functions $R_{mn}^{II}(r)$, $R_{mn}^{*II}(r)$ are presented in Appendix A.

(c)   Third fluid domain, Type III ($c \leq r \leq b$, $0 \leq z \leq d$):

$$\frac{1}{d}\Psi_{D,m}^{III} = \sum_{i=0}^{\infty} \left[R_{mi}^{III}(r)F_{mi}^{III} + R_{mi}^{*III}(r)F_{mi}^{*III} \right] Z_i(z) \tag{23}$$

where Z_i are orthonormal functions in $[0, d]$ defined by Equations (4) and (21) for $i = 0$, $i > 0$, respectively. The functions $R_{mi}^{III}(r)$, $R_{mi}^{*III}(r)$ are presented in Appendix A.

(d)   Fourth fluid domain, Type IV ($l \leq r \leq c$, $0 \leq z \leq d - h_2$):

$$\frac{1}{d}\Psi_{D,m}^{IV} = \sum_{s=0}^{\infty} \varepsilon_s \left[R_{ms}^{IV}(r)F_{ms}^{IV} + R_{ms}^{*IV}(r)F_{ms}^{*IV} \right] \cos\left(\frac{s\pi z}{d - h_2}\right) \tag{24}$$

Here ε_s stands for the Neumann's symbol and the functions $R_{ms}^{IV}(r)$, $R_{ms}^{*IV}(r)$ are defined in Appendix A.

(e)   Fifth fluid domain, Type V ($0 \leq r \leq l$, $0 \leq z \leq d$):

$$\frac{1}{d}\Psi_{D,m}^{V} = \sum_{q=0}^{\infty} F_{mq}^{V} \frac{I_m(a_q r)}{I_m(a_q l)} Z_q(z) \tag{25}$$

where Z_q are orthonormal functions in $[0, d]$ defined by Equations (4) and (21) for $q = 0$, $q > 0$, respectively, whereas the term I_m is the mth order modified Bessel function of the first kind. We note that the modified Bessel function of second type $K_m(a_q r)$ does not appear in the velocity potential representation of this fluid domain type, as the function K_m has a singular behavior at $r \to 0$. The latter has namely a contribution proportional to $(l/r)^m$ for $m \neq 0$ and $\log(r)$ for $m = 0$ at $r \to 0$ [32].

Based on the derived velocity potentials in each fluid domain, the continuity requirements of the hydrodynamic pressure and radial velocity at the boundaries of neighboring fluid regions, expressed through Equations (12)–(19), along with the kinematic boundary conditions at the vertical walls of the body, are then to be fulfilled (see Equation (10)). Hence, the linear system of equations for the determination of the unknown Fourier coefficients F_{mj}^l, $l = I, II, III, IV, V$, and F_{mj}^{*s}, $s = II, III, IV$, in each fluid domain, was derived. The solution procedure is presented in the following Section 2.2.

2.2. Solution Procedure

In this subsection, the solution procedure for determining the unknown Fourier coefficients in each fluid domain is presented. Towards this goal, we first expressed the velocity potentials of the fluid domains at their vertical boundaries. To this end, by accounting for the values of the functions $R_{mn}^{II}(r)$, $R_{mn}^{*II}(r)$, $R_{mi}^{III}(r)$, $R_{mi}^{*III}(r)$, $R_{ms}^{IV}(r)$, $R_{ms}^{*IV}(r)$ (see Appendix A) at $r = a$, b, c and $r = l$, the potential functions $\Psi_{D,m}^i$, $i = I, II, III, IV, V$, see Equations (20), (22)–(25), can be reduced to the following simple series expressions at $r = a, b, c, l$:

$$\frac{1}{d}\Psi_{D,m}^{I}(a, z) = \sum_{j=0}^{\infty} F_{mj}^{I} Z_j(z) \tag{26}$$

$$\frac{1}{d}\Psi_{D,m}^{II}(a, z) = \sum_{n=0}^{\infty} \varepsilon_n F_{mn}^{II} \cos\left(\frac{n\pi z}{d - h_1}\right) \tag{27}$$

$$\frac{1}{d}\Psi_{D,m}^{II}(b,z) = \sum_{n=0}^{\infty} \varepsilon_n F_{mn}^{*II} \cos\left(\frac{n\pi z}{d-h_1}\right) \tag{28}$$

$$\frac{1}{d}\Psi_{D,m}^{III}(b,z) = \sum_{i=0}^{\infty} F_{mi}^{III} Z_i(z) \tag{29}$$

$$\frac{1}{d}\Psi_{D,m}^{III}(c,z) = \sum_{i=0}^{\infty} F_{mi}^{*III} Z_i(z) \tag{30}$$

$$\frac{1}{d}\Psi_{D,m}^{IV}(c,z) = \sum_{s=0}^{\infty} \varepsilon_s F_{ms}^{IV} \cos\left(\frac{s\pi z}{d-h_2}\right) \tag{31}$$

$$\frac{1}{d}\Psi_{D,m}^{IV}(l,z) = \sum_{s=0}^{\infty} \varepsilon_s F_{ms}^{*IV} \cos\left(\frac{s\pi z}{d-h_2}\right) \tag{32}$$

$$\frac{1}{d}\Psi_{D,m}^{V}(l.z) = \sum_{q=0}^{\infty} F_{mq}^{V} Z_q(z) \tag{33}$$

Next, by taking into consideration Equations (26)–(33), which represent the velocity potential at the vertical boundaries of the various fluid regions, as well as Equations (12), (14), (16), (18), which express the conditions for continuity of the potential function at $r = a$, b, c, l, we multiply both sides of Equations (12) and (14) by $1/(d-h_1)\cos(v\pi z/(d-h_1))$, $v = 0, 1, 2, \ldots, n \ldots$, and of Equations (16) and (18) by $1/(d-h_2)\cos(v\pi z/(d-h_2))$, $v = 0, 1, 2, \ldots, s \ldots$, and then we integrate the resulting expressions over their regions of validity. The resulting expressions relating the Fourier coefficients of adjacent fluid regions are:

$$F_{ms}^{*IV} = \sum_{q=0}^{\infty} L_{sq} F_{mq}^{V} \tag{34}$$

$$F_{ms}^{IV} = \sum_{i=0}^{\infty} L_{si} F_{mi}^{*III} \tag{35}$$

$$F_{mn}^{*II} = \sum_{i=0}^{\infty} L_{ni} F_{mi}^{III} \tag{36}$$

$$F_{mn}^{II} = \sum_{j=0}^{\infty} L_{nj} F_{mj}^{I} \tag{37}$$

The $L_{sq}, L_{si}, L_{ni}, L_{nj}$ terms are defined in Appendix B.

Furthermore, the conditions for the continuity of the first derivatives of the potential at $r = a, b, c, l$ (see Equations (13), (15), (17) and (19)), as well as the kinematical boundary conditions at the body's vertical boundaries (see Equation 10), must also be fulfilled. Hence, multiplying both sides of Equations (10), (13), (15), (17) and (19) by $(1/d)Z_v(z)$, $v = 0, 1, 2, \ldots, q, \ldots$, integrating over the regions of their validity and adding the resulting expressions, the flowing set of equations can be obtained:

$$F_{mj}^{I}\Lambda_j^{I} = \frac{d-h_1}{d}\sum_{n=0}^{\infty} \varepsilon_n L_{nj}\left[\Lambda_{mn}^{II}F_{mn}^{II} + \Lambda_{mn}^{*II}F_{mn}^{*II}\right], \tag{38}$$

$$\text{for } r = a, \ 0 \le z \le d$$

$$\Lambda_{mi}^{III}F_{mi}^{III} + \Lambda_{mi}^{*III}F_{mi}^{*III} = \frac{d-h_1}{d}\sum_{n=0}^{\infty} \varepsilon_n L_{ni}\left[D_{mn}^{II}F_{mn}^{II} + D_{mn}^{*II}F_{mn}^{*II}\right], \tag{39}$$

$$\text{for } r = b, \ 0 \le z \le d$$

$$D_{mi}^{III}F_{mi}^{III} + D_{mi}^{*III}F_{mi}^{*III} = \frac{d-h_2}{d}\sum_{s=0}^{\infty} \varepsilon_s L_{si}\left[\Lambda_{ms}^{IV}F_{ms}^{IV} + \Lambda_{ms}^{*IV}F_{ms}^{*IV}\right], \tag{40}$$

$$\text{for } r = c, \ 0 \le z \le d$$

$$F_{mq}^V \Lambda_q^V = \frac{d - h_2}{d} \sum_{s=0}^{\infty} \varepsilon_s L_{sq} \left[D_{ms}^{IV} F_{ms}^{IV} + D_{ms}^{*IV} F_{ms}^{*IV} \right], \tag{41}$$

$$\text{for } r = l, \ 0 \leq z \leq d$$

The terms $\Lambda_j^I, \Lambda_q^V, \Lambda_{mn}^{II}, \Lambda_{mn}^{*II}, D_{mn}^{II}, D_{mn}^{*II}, \Lambda_{mi}^{III}, \Lambda_{mi}^{*III}, D_{mi}^{III}, D_{mi}^{*III}, \Lambda_{ms}^{IV}, \Lambda_{ms}^{*IV}, D_{ms}^{IV}, D_{ms}^{*IV}$ in Equations (38)–(41) are described in Appendix B.

The solution of the infinite system described by the linear Equations (34)–(37) and (38)–(41) will provide the unknown Fourier coefficients, F_{mj}^l, $l = I, II, III, IV, V$, and F_{mj}^{*s}, $s = II, III, IV$, in each fluid domain. It should be noted that for the numerical implementation of the method, infinite series (20), (22)–(25), are truncated after J, N, I, S, Q terms, respectively. A similar procedure has also been used in [1,5,6].

2.3. Hydrodynamic Exciting Forces/Moment and Wave Elevation

Having evaluated the diffraction velocity potential, the hydrodynamic pressure in each fluid region could be estimated by the linearized Bernoulli equation. Hence, the exciting forces and moments on the moonpool cylindrical body could be determined by integrating the hydrodynamic pressure, p, over the body's wetted surface, as follows:

$$F_k(t) = - \iint_{S_0} p n_k dS = -i\omega\rho e^{-i\omega t} \iint_{S_0} \varphi_D n_k dS$$

$$= -\omega^2 \rho \frac{H}{2} e^{-i\omega t} \sum_{m=0}^{\infty} \varepsilon_m i^m \iint_{S_0} \Psi_{D,m}(r,z) \cos(m\theta) n_k dS, \quad \text{for } k = 1,3 \tag{42}$$

and

$$F_5(t) = M_1(t) + M_3(t) \tag{43}$$

where:

$$M_k(t) = - \iint_{S_0} p(r \times n_k) dS = -i\omega\rho e^{-i\omega t} \iint_{S_0} \varphi_D(r \times n_k) dS$$

$$= -\omega^2 \rho \frac{H}{2} e^{-i\omega t} \sum_{m=0}^{\infty} \varepsilon_m i^m \iint_{S_0} \Psi_{D,m}(r,z) \cos(m\theta)(r \times n_k) dS, \quad \text{for } k = 1,3 \tag{44}$$

Here S_0 is the mean wetted surface of the body; ρ is the water density; n_k are the generalized normal components defined by $\mathbf{n} = (n_1, n_2, n_3)$; $r \times \mathbf{n} = (n_4, n_5, n_6)$, r being the position vector of a point on the wetted surface with respect to the reference co-ordinate system of the body. Analytical representations of the exciting forces and moments on the body are presented in Appendix C.

The free surface elevation outside and in the annulus and moonpool areas inside the body is given by the linearized boundary condition on the free surface (see Equation (7)). It holds:

$$Z(r, \theta, z; t) = Re\left\{ \zeta(r, \theta, d) e^{-i\omega t} \right\} = Re\left\{ \frac{i\omega}{g} \varphi_D(r, \theta, d)(\cos(\omega t) - i\sin(\omega t)) \right\} \tag{45}$$

3. Computation Fluid Dynamics—MaPFlow Solver

In this section, a brief description of the CFD modelling applied to the present bodies' configurations is presented. For a more detailed review of the solver's methodology, the reader may refer to [29,33]. In the previous mentioned publications, a series of test cases have been examined, including a moonpool configuration excited by incident waves that prove the liability of the solver in this type of simulations.

MaPFlow treats free surface flows as flows of two immiscible and incompressible fluids. The presence of the two fluids is described using the Volume of Fluid (VoF) approach [34], while the requirement of the incompressibility is satisfied using the artificial compressibility method (ACM) [35]. The governing equations are presented in Equation (46). The system of equations, in 3 dimensions, consists of 5 scalar equations. The equations are augmented

by the pseudo-time derivatives of the variables. The aim of the numerical procedure is to drive these derivatives to zero; thus the original unsteady system of equations will be retrieved. The coupling of the equations is performed during the pseudo-time, where a relation between the density and the pressure field is assumed. The coupling is controlled through the relation $\frac{\partial \rho}{\partial p}\big|_\tau = \frac{1}{\beta}$, where β is a free parameter that in typical free surface flows ranges from 5 to 15 [33,36].

$$\Gamma \int_\Omega \frac{\partial \vec{Q}}{\partial \tau} d\Omega + \Gamma_e \int_\Omega \frac{\partial \vec{Q}}{\partial t} d\Omega + \int_{\partial \Omega} \left(\vec{F}_c - \vec{F}_v \right) dS = \int_\Omega \vec{S}_q d\Omega \tag{46}$$

In the above integral equation, Ω is a control volume with boundary $\partial \Omega$, $\vec{Q} = [p, \vec{u}, a]^T$ is the vector of the unknown variables (pressure p, velocity $\vec{u}$ and volume fraction a), vector $\vec{S}_q$ contains the various source terms of the equations such as the gravitational field, while t and τ denote the real and fictitious time, respectively. The original ACM when applied to two-phase flows scales locally with the density field and this results to a stiff numerical behavior. In order to remedy this dependency, the preconditioner Γ of Kunz [37] is used; it is presented in Equation (47). Furthermore, to recover the conservative form of the equations, the unsteady terms of Equation (46) are supplemented with the matrix Γ_e, which is also presented in Equation (47).

$$\Gamma = \begin{bmatrix} \frac{1}{\beta \rho_m} & 0 & 0 \\ 0 & \rho_m I & \vec{u} \Delta \rho \\ \frac{\alpha}{\beta \rho_m} & 0 & 1 \end{bmatrix}, \quad \Gamma_e = \begin{bmatrix} 0 & 0 & 0 \\ 0 & \rho_m I & \vec{u} \Delta \rho \\ 0 & 0 & 1 \end{bmatrix} \tag{47}$$

Finally, $\vec{F}_c$ is the vector of the convective fluxes and $\vec{F}_v$ the vector of the viscous fluxes. The two vectors are given by Equation (48).

$$F_c = \begin{bmatrix} V_n \\ \rho_m u \Delta V + p n_x \\ \rho_m v \Delta V + p n_y \\ \rho_m w \Delta V + p n_z \\ a V_n \end{bmatrix}, \quad F_v = \begin{bmatrix} 0 \\ \tau_{xx} n_x + \tau_{xy} n_y + \tau_{xz} n_z \\ \tau_{yx} n_x + \tau_{yy} n_y + \tau_{yz} n_z \\ \tau_{zx} n_x + \tau_{zy} n_y + \tau_{zz} n_z \\ 0 \end{bmatrix} \tag{48}$$

In Equation (48), ΔV is the velocity difference between the contravariant velocity $V_n = \vec{u} \cdot \vec{n}$ and the grid face velocity due to the mesh motion $V_g = \vec{u}_{vol} \cdot \vec{n}$. In the present study, because the structures were considered fully restrained, the mesh was stationary; thus, $V_g = 0$. Furthermore, the viscous fluxes are computed through the viscous stresses τ_{ij}, which in turn were expressed using the Boussinesq approximation, by Equation (49).

$$\tau_{ij} = (\mu_t + \mu_m) \left(\frac{\partial u_i}{\partial x_j} + \frac{\partial u_j}{\partial x_i} \right) - \frac{2}{3} \rho_m k \delta_{ij} \tag{49}$$

In the above equation, μ_m is the viscosity of the mixture, μ_t is the turbulent viscosity, k the turbulent kinetic energy and δ_{ij} the Kronecker's symbol. Moreover, since here only small amplitude linear waves were investigated, the turbulence modelling was switched off ($\mu_t = 0$, $k = 0$).

The generation and damping of the free surface waves were performed by adding source terms to the momentum equations in user-specified regions near the boundaries of the computational domain. The form of this source term is described by Equation (50). The source terms scale according to the coefficient C_{nwt}, which is controlled though the factor $\alpha_{nwt} \left[\frac{1}{s} \right]$ and the function $f(x_{nwt})$ defined inside the wave generation or damping zone. $f(x_{nwt})$ has typically an exponential or polynomial form [38]; α_{nwt} is a free parameter that depends on the flow itself (e.g., the waves entering the damping zone) and the discretization

process. In [33], a parametric analysis of the effects of the coefficient C_{nwt} is presented. The source term $\vec{S}_{nwt}$ drives the solution to the desired velocity field $\vec{u}_{tar}$. The target velocity in the case of generation zone was the velocity field provided by an analytical solution of free surface waves (linear, Stokes nth order waves, etc.); in the case of damping zone, the usual strategy was to set the normal velocity to the boundary equals to zero.

$$\vec{S}_{nwt} = C_{nwt}\rho_m \left(\vec{u} - \vec{u}_{tar} \right), \qquad C_{nwt} = \alpha_{nwt} f(x_{nwt}) \tag{50}$$

The above system of equations was discretized using the finite volume method. In each cell of the computational mesh, a control volume Ω_I was defined, where the unknown variables had a constant value and the control volume was represented by the geometric center of the computational mesh (cell-centered approximation). The surface integrals were decomposed into a sum of constant surface integral over the faces that make up the cell. The semi-discretized form of the equations is presented in Equation (51). The source terms of the equations are considered constant in each cell.

$$\Gamma_e \frac{\partial \left(\vec{Q}\Omega_I \right)}{\partial t} + \Gamma\Omega_I \frac{\partial \vec{Q}}{\partial \tau} = -\vec{R}_{\Omega_I} \tag{51}$$

$\vec{R}_{\Omega_I}$ is the spatial residual of the discretization process (see Equation (52)).

$$\vec{R}_{\Omega_I} \simeq \sum_{j}^{N_f(\Omega_I)} \left(\vec{F}_c - \vec{F}_v \right)_j \Delta S_j + \Omega_I \vec{S}_q \tag{52}$$

The convective fluxes are computed using the approximate Riemann solver of Roe [39,40], whereas a second order interpolation scheme supplemented by a directional derivative to account for the skewness of the mesh has been applied for the computation of the viscous fluxes.

For the time discretization, a second order backwards differentiation scheme was used [41] for the real time derivatives, while, for the pseudo-time derivatives, a first order explicit Euler scheme was utilized. In order to facilitate convergence, the pseudo-timestep scales locally in each cell based on a given Courant-Friedrichs-Lewy (CFL) number and the characteristics of the flow. For an analytic description of the time discretization process the reader can refer to [33].

Finally, regarding the boundary conditions, at the wall boundaries, the no-slip boundary condition was applied; the symmetry plane was treated as a slip boundary, while the far field boundaries were approximated using ghost cells. At every far field boundary face, an approximate Riemann problem was solved between the state inside the domain and the far field conditions imposed by the ghost cell. It should be noted that, in the case of wave generation, the ghost cell's values were given by the current wave solution.

The discretization of the equations led to a non-linear system of equations. The linearization process took places in pseudo-time. The resulting linear system was solved using a Gauss–Seidel iterative method, while it was permutated using the Reverse Cuthill-Mckee reordering scheme to accelerate convergence.

The above methodology was implemented as part of the CFD solver MaPFlow [42,43]; MaPFlow was developed in NTUA, solved the URANS equations in unstructured meshes and is capable of running up to 1000 parallel processes utilizing the MPI protocol.

4. Results

In accordance with the procedure presented in the previous sections, it is obvious that the accuracy of the method and the CPU time required was affected by the evaluation procedure of the Fourier coefficients in each fluid domain. In the present calculations, 80 terms were used for the series expansions of the velocity potential in the fluid domains

of the *I, III* and *V* types, whilst 150 terms are retained for the velocity representation in the *II, IV* types.

Two different geometric configurations of a moonpool-type floater were investigated; a floater encompassed by two coaxial, free-surface piercing moonpool cylinders with vertical symmetry axes (Configuration 1, see Figure 1a) and a floater consisting of an external toroidal cylinder and an internal coaxial surface piercing truncated circular cylinder (Configuration 2, see Figure 1b) [30]. Specifically, for the Configuration 1 (i.e., coaxial hollow cylinders) it held: $\alpha = 13$ m, $b = 12$ m, $c = 9$ m, $l = 6.083$ m, and $h_1 = 14$ m, $h_2 = 5.5$ m (see Figure 2a), whereas, for the Configuration 2 (i.e., coaxial truncated cylinder), it was assumed: $\alpha = 13$ m, $b = 12$ m, $c = 9$ m, $h_1 = 14$ m and $h_2 = 5.5$ m (see Figure 2b). Both arrangements were considered restrained to the wave impact at a water depth of $d = 70$ m.

(a)   (b)
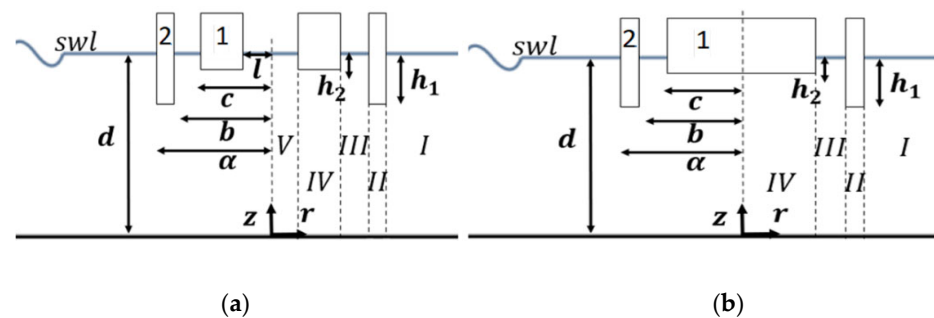
Figure 2. Schematic representation of the two moonpool-type case studies: (**a**) floater of two coaxial, free-surface piercing moonpool cylinders with vertical symmetry axes; (**b**) floater of an external toroidal cylinder and an internal coaxial truncated cylinder.

Regarding the numerical results that were produced by the in-house CFD solver, the two different configurations were excited by linear waves with wave frequencies ranging from 0.6 rad/s to 1.2 rad/s, with a constant wave height of 0.6 m. Based on the linear wave theory of Airy, the velocity field of the wave was imposed on the one end of the domain, while, at the other end, wave damping was used. The waves were propagated along the x-axis, while the free surface was placed perpendicular to the z-axis. In order to save computational resources, only the half domain was simulated by setting symmetry boundary conditions to the xz-plane. Due to the large deviation of the wave lengths, two different computational domains were used, for each case. For wave frequencies between 0.6 and 0.8 rad/s (which corresponds to wave lengths between 170 to 95 m, respectively) the domain had a total length of 600 m, while, for the wave frequencies between 0.85 and 1.20 rad/s (where the wave lengths range between 85 and 45 m), a domain of total length of 300 m is used.

The domain discretization is depicted in Figure 3. The discretization of the domain upwind of the configuration was based on the wave characteristics. Near the free surface, the domain was uniform along the z-axis, with a length that corresponded to 18 cells per wave height. The mesh along the wave propagation was also uniform, with a discretization that corresponded to at least 100 cells per wavelength in each domain for the studied wave frequencies. Furthermore, special care was taken near the sharp edges of the structure, as illustrated in Figure 3a, to account for the flow separation that was expected in these regions. Finally, the mesh coarsened as it reached the lateral and the outflow boundary, to make sure that no wave reflections occurred. In order to capture the viscous effects close to the wall, the first point was placed at 0.5 mm normal to the wall.

(a)

(b)

(c)
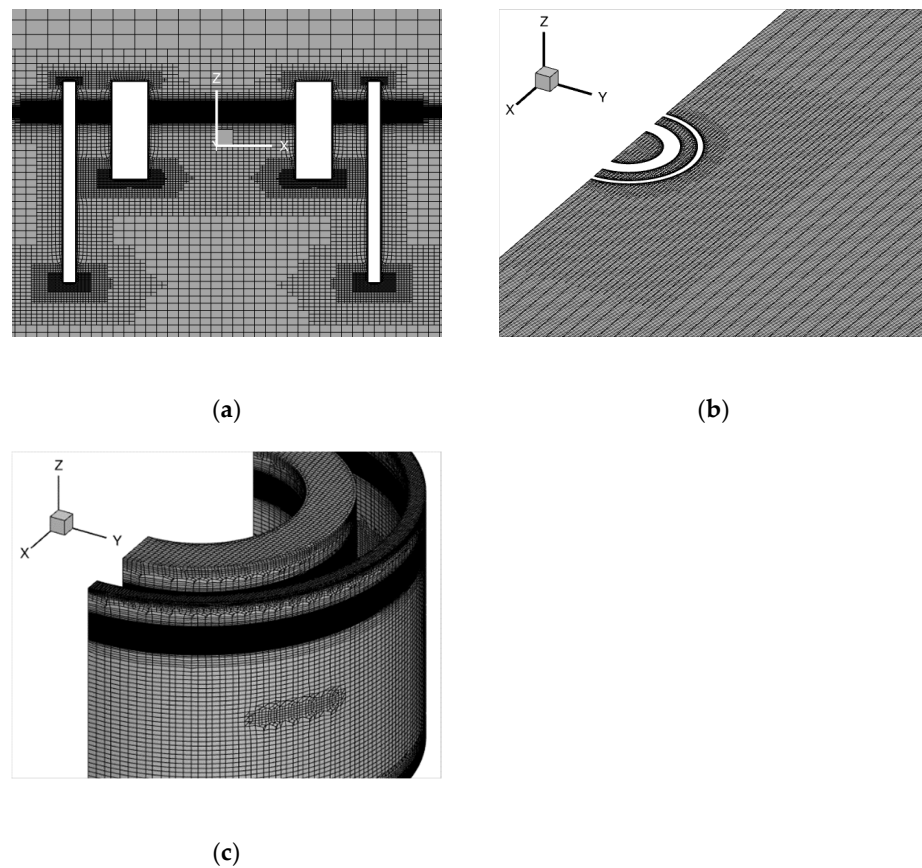
Figure 3. Computational mesh used for the CFD simulations, in case of Configuration 1. The mesh of the Configuration 2 has the corresponding characteristics; (**a**) symmetry plane; (**b**) z plane cut; (**c**) surface mesh.

Figure 4 presents the grid independency study. The M2 grid has the aforementioned mesh characteristics and a total size of approximately 5 million cells. Additionally, three more grids were examined. The M1 grid consisted of 1.6 million cells. The main difference compared to the M2 grid is that it had 8 cells along the wave height and 50 cells at the smallest wavelength. Furthermore, the characteristic size of the mesh close to the wall is two times larger, compared to the previous mesh. The M2-w mesh had the same characteristics as the M2 grid; however, the first node from the wall was placed at 1 mm normal to the wall. Finally, the M3 had a total size of 8.5 million cells. The M3 grid differed from M2 in the characteristics of the mesh near the structure, as well as upwind of the structure in the direction of the wave propagation. The cells per wave height were the same as M2; the total cells per smallest wavelength were 200; the mesh near the structure had two times smaller characteristic size. From the independency study, the M2, M2-w and M3 produced similar results. The characteristics of the M2 grid were chosen for all simulations. The time discretization was chosen as 1000 timesteps for the corresponding wave period [33].

(**a**)　　　　　　　　　　　　　　　　　　　　(**b**)
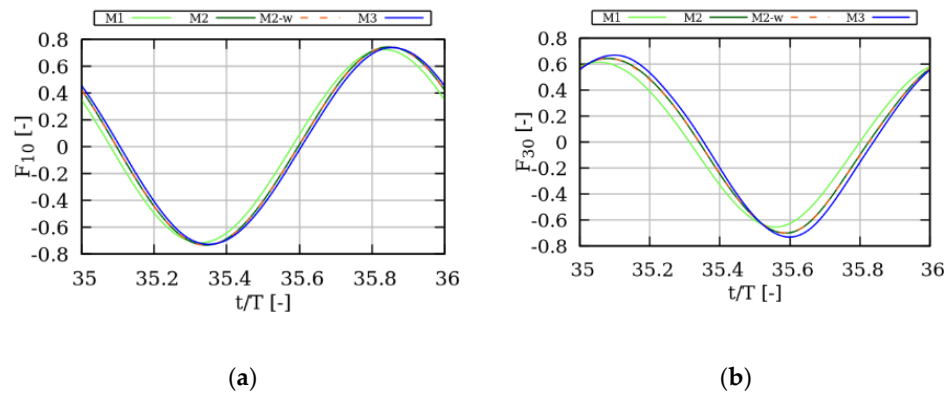
Figure 4. Grid Independency study. Forces acting on Configuration 2 during the 35th wave period. The wave excitation frequency is $\omega = 0.80$ rad/s; (**a**) horizontal excitation force; (**b**) vertical excitation force.

Figures 5 and 6 depict the horizontal and vertical exciting forces on the moonpool floater of the 1st examined Configuration, derived by the presented potential flow formulation. The results are also compared with the corresponding exciting forces on the outer moonpool floater (i.e., Body 2) (see Figure 2a), without the presence of the inner moonpool floater (i.e., Body 1), as well as on Body 1, without the presence of Body 2 (i.e., isolated bodies). The results of the exciting forces are normalized by the term $\pi \rho g \alpha^2 (H/2)$.
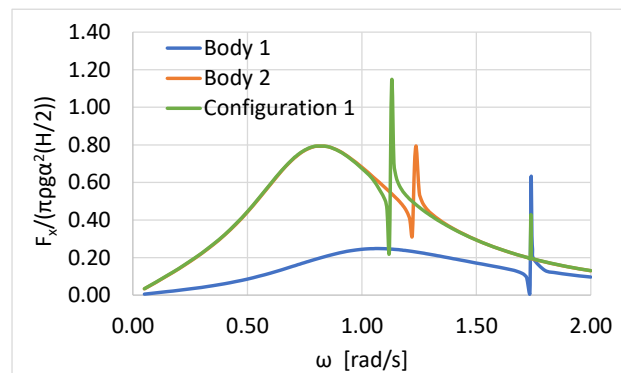
Figure 5. Horizontal exciting forces on the Configuration 1. The results are also compared with the corresponding forces on the isolated toroidal Bodies 1 and 2.
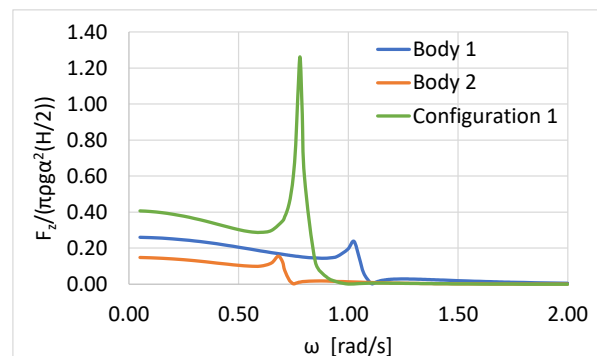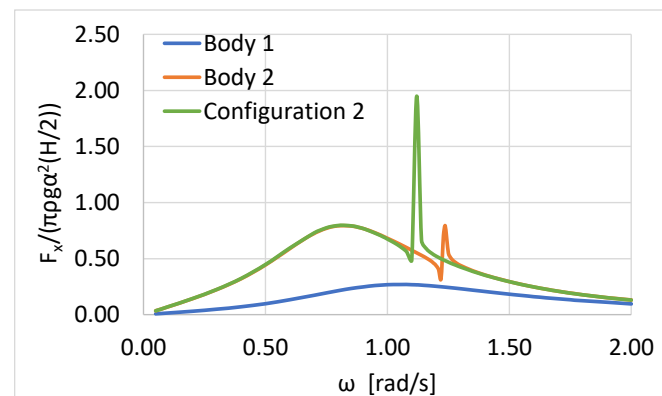

Figure 6. Vertical exciting forces on the Configuration 1. The results are also compared with the corresponding forces on the isolated toroidal Bodies 1 and 2.

The peculiar behavior of the horizontal exciting forces (see Figure 5) on the Body 1 and Body 2, in the neighborhood of $\omega \sim 1.74$ rad/s and $\omega \sim 1.23$ rad/s, respectively, was due to the resonance pitch oscillations of the interior water basin of each Body 1 and 2. The same behavior has been reported in [1] regarding moonpool floaters. It should be further noted

that the peculiar behavior of the horizontal exciting force on the total Configuration 1 (i.e., floater of two coaxial, free-surface piercing toroidal cylinders) was moved at a lower wave frequency, i.e., $\omega \sim 1.13$ rad/s. This transpose could be attributed to the annular water area that formed between the two toroidal cylinders, which resonated in a pitch at a lower wave frequency than the corresponding one of the independent moonpool floaters (i.e., Body 1 and Body 2). In addition, a secondary resonance of the horizontal exciting force on the total Configuration 1 was observed in the neighborhood of $\omega \sim 1.74$ rad/s. In the latter wave frequency, the resonance pitch oscillations of the interior water basin inside the Body 1 occurred.

With regard to the vertical forces (see Figure 6) on Body 1 and Body 2, resonances appeared in the vicinity of $\omega \sim 1.05$ rad/s and $\omega \sim 0.7$ rad/s, respectively. These peaks were due to the pumping resonance of the fluid motion in the interior water area of the moonpools Body 1 and Body 2. Concerning the vertical exciting force on the total Configuration 1, it can be seen (Figure 6) that its pumping resonant wave frequency was located in between the corresponding pumping wave frequencies of Body 1 and Body 2 (i.e., $\omega \sim 0.8$ rad/s).

Next, the horizontal and vertical wave exciting forces on the examined Configuration 2 (see Figure 2b), derived from the theoretical formulation, are presented. Specifically, in Figures 7 and 8 the values of $F_x/(\pi \rho g \alpha^2 (H/2))$ and $F_z/(\pi \rho g \alpha^2 (H/2))$ on the Configuration 2 are depicted, respectively. The results are also compared with the corresponding exciting forces on the isolated Body 1 and Body 2, when the latter were considered alone in the wave field (i.e., Body 1 was assumed alone in the wave field without the presence of Body 2, and vice versa for Body 2).

Figure 7. Horizontal exciting forces on the Configuration 2. The results are also compared with the corresponding forces on the isolated Bodies 1 and 2.
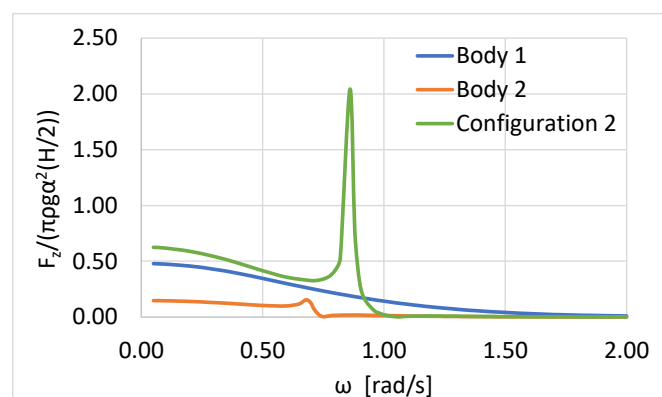
Figure 8. Vertical exciting forces on the Configuration 2. The results are also compared with the corresponding forces on the isolated Bodies 1 and 2.

The resonance of the horizontal exciting force on the Configuration 2 (see Figure 7), which occurred in the neighborhood of ω ~ 1.125 rad/s due to the pitch fluid motion in the annular fluid area between the interior cylinder and the exterior toroidal body, was moved to ω ~ 1.24 rad/s for the Body 2 case, when the latter was assumed isolated in the wave field. As far as the forces on the isolated Body 1 are concerned, it can be seen that they followed a smooth variation pattern at the examined wave frequency range, without any sharp maximizations.

Regarding the vertical exciting forces on the Configuration 2 (see Figure 8), the pumping resonance of the fluid motion in the annular area was depicted at ω ~ 0.85 rad/s [20], whereas, for the isolated Body 2, this pumping resonance lied near ω ~ 0.7 rad/s (see discussion of Figure 5). It should also be noted that the smooth variation pattern of the vertical exciting force on the isolated cylinder follows (i.e., Body 1).

Comparing Figures 5 and 7, it can be concluded that both configurations 1 and 2 attained, in the non-resonance regime, comparable results concerning the horizontal exciting wave forces. Furthermore, their resonance pitch oscillations occurred at the vicinity of ω ~ 1.13 rad/s. Hence, it could be derived that the wave motion inside the pond of Body 1 in the first configuration did not seem to affect the floater's horizontal forces. On the other hand, the secondary resonance of the horizontal exciting wave force on the Configuration 1 (i.e., ω~1.74 rad/s) was not observed in the case of Configuration 2. Regarding the vertical exciting forces $F_z/(\pi\rho g\alpha^2(H/2))$, see Figures 6 and 8; in the case of Configuration 2, due to the truncated inner cylindrical body, they attained higher values compared to the vertical loads on Configuration 1. Hence, assuming both Configurations as heaving point absorbers for wave energy exploitation, Configuration 2 seems to be more efficient compared to Configuration 1.

In the sequel, the results from the theoretical formulation were supplemented by numerical ones, which took into consideration the viscous effects near the sharp edges of the examined moonpool-type floaters. The numerical results presented follow the configuration terminology described in the previous section. A grid consisting of 5 million cells was employed with symmetry conditions (half of the moonpool is modelled). Since the moonpool was considered fixed and the waves were essentially in the linear region, the flow is assumed laminar [29,44].

Regarding Configuration 1 the comparison of the non-dimensional horizontal and vertical exciting forces could be seen in Figures 9 and 10. The illustration of the horizontal forces (Figure 9) suggested that the comparison was relatively good for both methods. CFD predictions follow the analytical method's trends with minor discrepancies. In the proximity of the peak excitation frequency (between 1.0–1.2 rad/s), the differences between the predictions became larger. More specifically, in the near peak frequency region, CFD results predicted earlier the peak of the Body 1 than the analytical method, leading to a rise in total force. At 1.13 rad/s, both methods predicted the maximum horizontal excitation force. However, it was evident that the amplitude of the CFD predictions was significantly smaller. This could be justified by both the phase difference of the peak excitation loads between the two bodies in the CFD predictions (discussed in the following) induced by the viscous effects that were taken into account in the CFD computations.
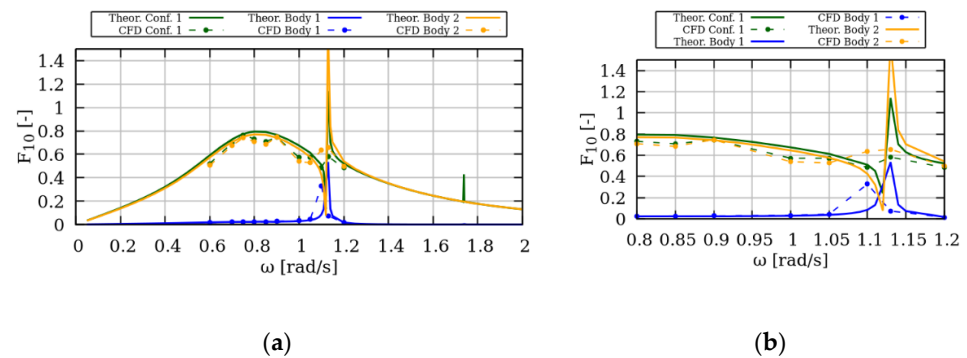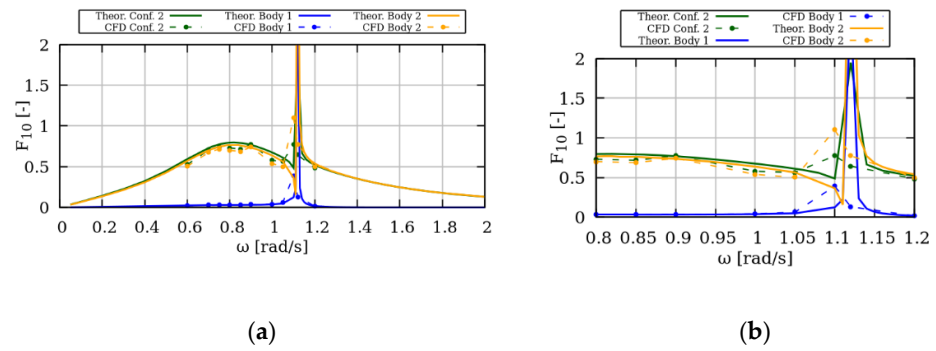
Figure 9. Comparison between the theoretical and CFD results of the non-dimensional horizontal excitation force, in case of the Configuration 1; (**a**) wave frequencies between 0.05 and 2 rad/s; (**b**) wave frequencies between 0.8 and 1.2 rad/s (detailed view).
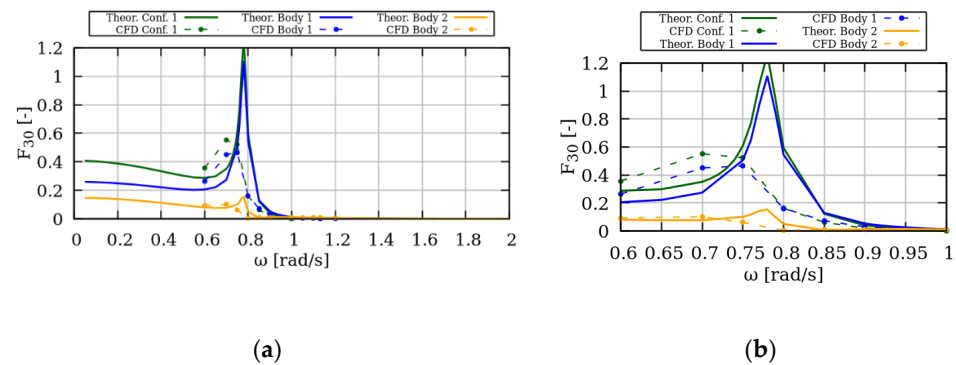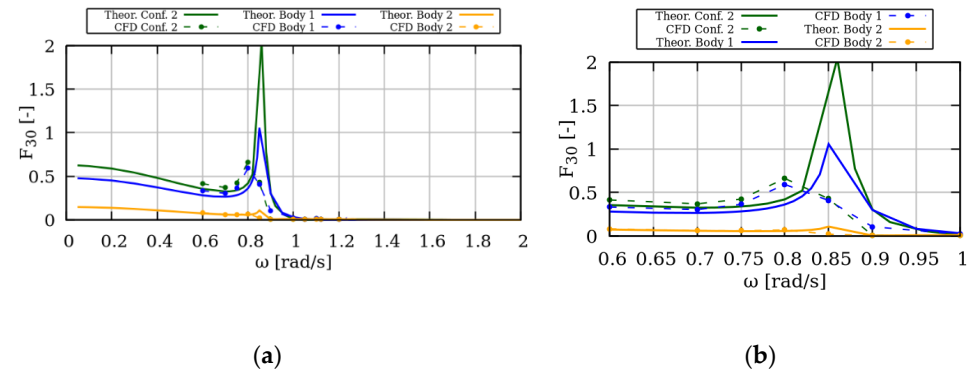

Figure 10. Comparison between the theoretical and CFD results of the non-dimensional vertical excitation force, in case of the Configuration 1; (**a**) wave frequencies 0.05 and 2 rad/s; (**b**) wave frequencies between 0.6 and 1.0 rad/s (detailed view).

Regarding the vertical excitation force in Figure 10, the comparison between the methodologies was fair, with the CFD simulations predicting smaller peak loads and shifted towards the lower frequencies. This has also been noted in [29]. Nevertheless, the qualitative comparison for both the total force and the individual body forces was considered to be in good agreement.

The respective comparison for Configuration 2 (external toroidal cylinder with internal coaxial truncated cylinder) can be found in Figures 11 and 12. The agreement between the numerical results is good in both the horizontal and vertical forces. As Figure 11 suggests, CFD predictions followed the analytical method trends; nevertheless, the peak excitation frequency was predicted earlier. As opposed to Configuration 1, the individual body forces peak excitation frequencies were predicted in the same frequency, suggesting that the forces on the two bodies were in phase. This was also the case for the analytical method's predictions. Finally, regarding the vertical force in Figure 12, again the CFD predicted the peak excitation frequency earlier; however, as in Configuration 1, the predicted trends were the same.

(**a**)   (**b**)

Figure 11. Comparison between the theoretical and CFD results of the non-dimensional horizontal excitation force, in case of the Configuration 2; (**a**) wave frequencies 0.05 and 2 rad/s; (**b**) wave frequencies between 0.8 and 1.2 rad/s (detailed view).


(**a**)   (**b**)

Figure 12. Comparison between the theoretical and CFD results of the non-dimensional vertical excitation force, in case of the Configuration 2; (**a**) wave frequencies 0.05 and 2 rad/s; (**b**) wave frequencies between 0.6 and 1.0 rad/s (detailed view).

In order to gain a better insight of this phase difference between each body's horizontal force in Configuration 1, instantaneous free surface elevation contours at four snapshots of the wave period are presented in Figure 13 at $\omega = 1.1$ rad/s.


(**a**)   (**b**)

Figure 13. *Cont.*

(**c**)　　　　　　　　　　　　　　　　　　　　　　　　(**d**)
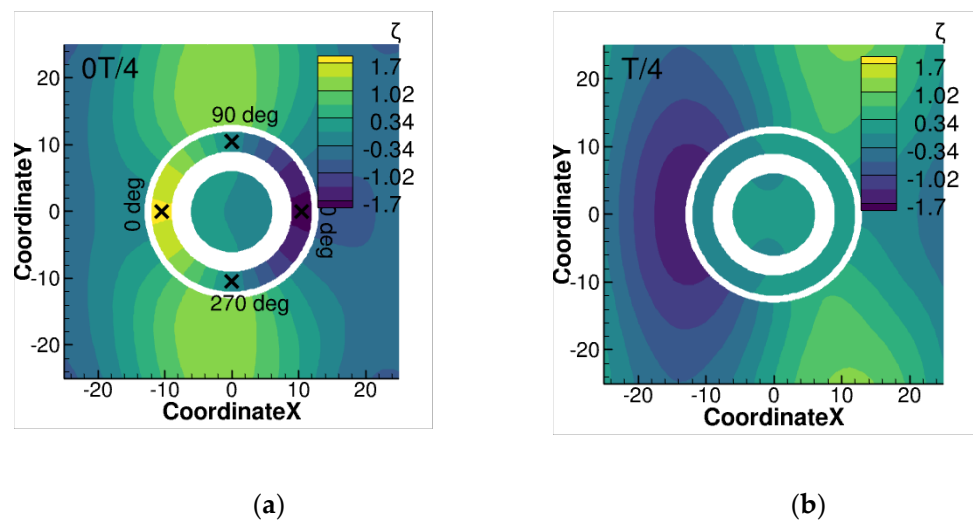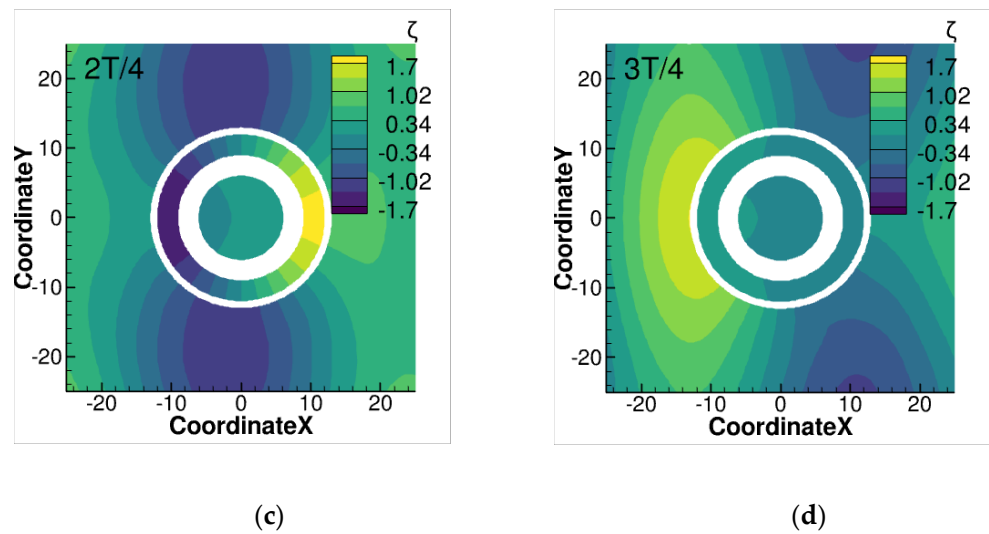
Figure 13. Snapshots of the non-dimensional surface elevation ($\zeta/(H/2)$) during a wave period for Configuration 1 and $\omega = 1.1$ rad/s; (**a**) t = 0T/4; (**b**); t = T/4; (**c**) t = 2T/4; (**d**) t = 3T/4.

As Figure 13 suggests, the sloshing mode was excited between the outer (Body 1) and the inner (Body 2) cylinder, which explains the phase difference between the horizontal force of each individual body.

Figure 14 presents the free surface elevations inside the moonpool (between Body 1 and 2) for both configurations with respect to the incident wave frequency. The space averaged free surface elevation inside the moonpool is presented, as well as in three circumferential positions at 0, 90 and 180 degrees (as shown in Figure 13a). In both configurations up to $\omega = 1$ rad/s, it was evident that the free surface elevation did not greatly vary between the various spatial positions, suggesting that the piston mode dominated the free surface elevation inside the moonpool. As the frequency increased beyond 1 rad/s the gauge at 90 degrees followed the spaced averaged elevation; however, the other two locations at 0 and 180 degrees clearly deviated (they increase in amplitude), thus indicating the appearance of a sloshing mode inside the moonpool. As the radial frequency was further increased, this mode dampens out. Furthermore, it is worth noting that peak frequencies of the piston mode resulted in an increase of the vertical forces, while the sloshing mode resulted in the resonance of the horizontal excitation forces.

(**a**)　　　　　　　　　　　　　　　　　　　　　　　　(**b**)
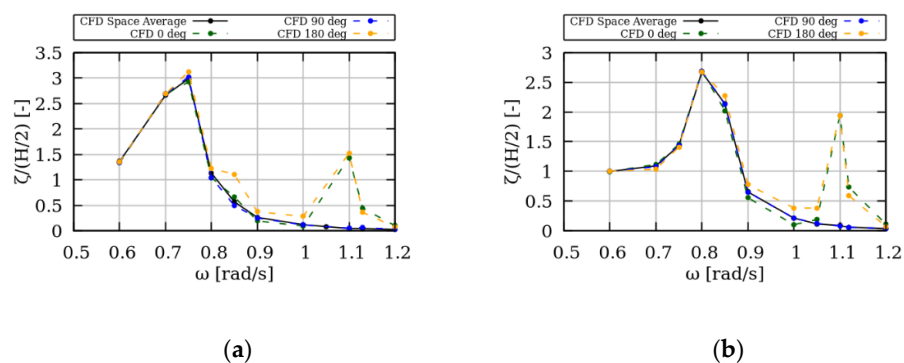
Figure 14. Analysis of the instantaneous free surface elevations inside the moonpool of Configuration 1 (**a**) and Configuration 2 (**b**) The position of the wave gauges is shown in Figure 13a. The non-dimensional amplitude of the free surface elevation ($\zeta/(H/2)$) is plotted for the various wave frequencies.

This is further illustrated in Figure 15, where the phase angle of the signal in the three wave gauges is presented. In smaller frequencies, the three signals had no phase

difference; however, in larger frequencies, the phases started to deviate. In the case of $\omega = 1.1$ rad/s, the signal in the upwind gauge (0 deg) and in the downwind gauge (180 deg) had a 90 degrees phase difference compared to the middle gauge (90 deg) and 180 degrees between them. In higher frequencies, there were still some phase differences; however, the amplitude of free surface was relatively small (see Figure 13).

(**a**)

(**b**)
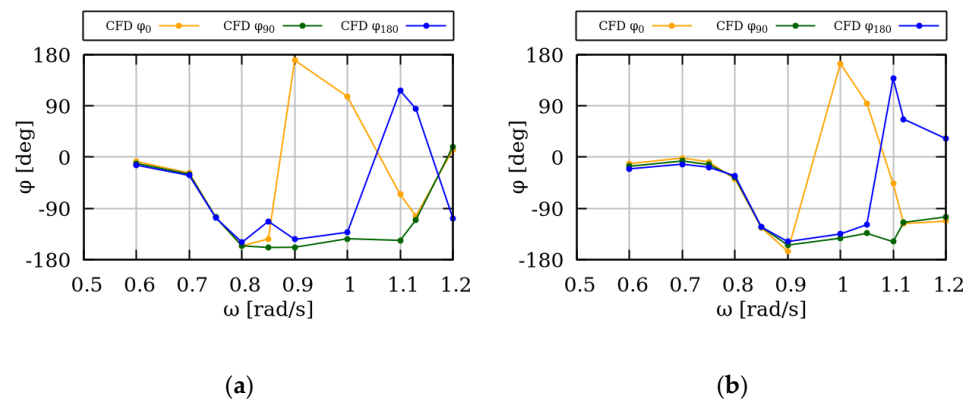
Figure 15. Analysis of the phase angle of the downwind (0 deg), middle (90 deg) and the upwind (180 deg) wave gauges for the two configurations. The position of the gauges is shown in Figure 13a; (**a**) Configuration 1; (**b**) Configuration 2.

Lastly, Figure 16 presents the y-vorticity field in the symmetry plane in the case of the Configuration 1 for different wave frequencies. Close to the resonance of the piston mode, excessive flow separation was noted near the sharp edges of the structure (Figure 16b). Due to the loss of energy in this region of recirculating flow, the viscous solver predicted smaller amplitude of the piston mode (and thus of the vertical forces) compared to the one of the analytical solution. Contrary to Figure 16b, the vorticity field in larger frequencies (where the amplitude of the piston mode is reduced significantly), the vortex shedding was not significant; thus, minor discrepancies were noted between the two approaches. It was also noted that the performance of inviscid potential models is influenced by the radiation effect of the inner water area, leading to discrepancies between the viscous solver and the analytical solution.

(**a**)

(**b**)
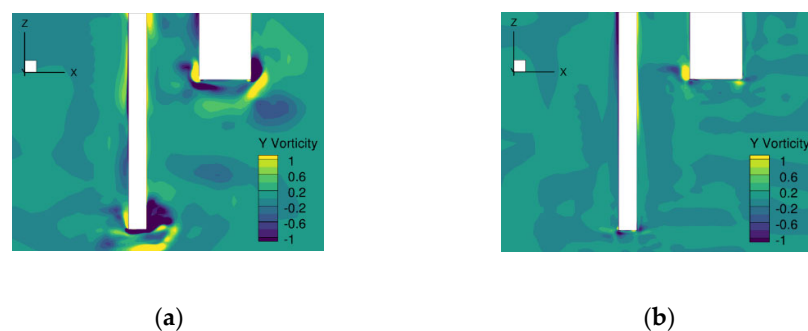
Figure 16. Snapshot of the y-vorticity field in the symmetry plane for two different wave frequencies, in case of Configuration 1; (**a**) vorticity field at the wave frequency where a resonant behavior of the piston mode is predicted ($\omega = 0.75$ rad/s); (**b**) vorticity field at the wave frequency where a resonant behavior of the pitch sloshing mode is predicted ($\omega = 1.1$ rad/s).

5. Conclusions

A semi-analytical method has been developed to solve the linearized diffraction problem of two types of moonpool floaters, namely: (a) two coaxial toroidal cylinders configuration and (b) a floater encompassed by an external toroidal cylinder and a coaxial internal truncated cylinder. The potential flow theoretical formulation was supplemented

by a numerical modelling that considered the viscous effects near the sharp edges of the body as non-negligible.

The accuracy of the two presented methods, the theoretical formulation and the numerical approximation, have been validated in both examined Configurations 1 and 2 and in a wide range of wave frequencies, i.e., 0.6 rad/s to 1.2 rad/s. It can be concluded that, in the non-resonance regime, the comparisons between the two methods were excellent; hence, both models predicted accurate results. However, in the critical wave frequencies near resonance, the CFD modelling predicted the peak excitation frequency earlier, whereas the amplitude of the predictions was significant smaller than the corresponding ones from the theoretical analysis. This can be traced back to the viscous effects that were taken into account in the CFD computations, which altered both the phase difference of the peak excitation loads between the two bodies in the CFD predictions. Specifically, an excessive flow separation was noted in the resonance regime, near the sharp edges of the structure; hence, the viscous solver predicted smaller force amplitudes. On the other hand, in larger frequencies the vortex shedding was negligible; thus, minor discrepancies were noted between the two approaches.

The present research will be continued further by comparing the accuracy of both methodologies to arrays of floating bodies in which the exciting forces on the structures are affected not only by the shape of the floaters but also from their position in the array towards the incoming waves.

Author Contributions: Conceptualization, S.A.M. and G.P.P.; methodology, A.S.M. and D.G.N.; software, S.A.M., D.G.N. and G.P.P.; validation, D.G.N. and A.S.M.; investigation, A.S.M., D.G.N., G.P.P. and D.N.K.; writing—original draft preparation, D.N.K.; writing—review and editing, S.A.M., G.P.P., D.G.N. and A.S.M.; visualization, D.N.K. and D.G.N.; supervision, S.A.M. All authors have read and agreed to the published version of the manuscript.

Conflicts of Interest: The authors declare no conflict of interest.

Appendix A

Expressions of the functions $R_{mn}^{II}(r)$, $R_{mn}^{*II}(r)$ in Equation (22):

$$R_{mn}^{II} = \frac{K_m\left(\frac{n\pi b}{d-h_1}\right)I_m\left(\frac{n\pi r}{d-h_1}\right) - K_m\left(\frac{n\pi r}{d-h_1}\right)I_m\left(\frac{n\pi b}{d-h_1}\right)}{K_m\left(\frac{n\pi b}{d-h_1}\right)I_m\left(\frac{n\pi a}{d-h_1}\right) - K_m\left(\frac{n\pi a}{d-h_1}\right)I_m\left(\frac{n\pi b}{d-h_1}\right)}, \ n \neq 0 \tag{A1}$$

$$R_{mn}^{*II} = \frac{K_m\left(\frac{n\pi r}{d-h_1}\right)I_m\left(\frac{n\pi a}{d-h_1}\right) - K_m\left(\frac{n\pi a}{d-h_1}\right)I_m\left(\frac{n\pi r}{d-h_1}\right)}{K_m\left(\frac{n\pi b}{d-h_1}\right)I_m\left(\frac{n\pi a}{d-h_1}\right) - K_m\left(\frac{n\pi a}{d-h_1}\right)I_m\left(\frac{n\pi b}{d-h_1}\right)}, \ n \neq 0 \tag{A2}$$

whereas, for $n = 0$ the terms R_{m0}^{II}, R_{m0}^{*II}, equal to:

$$R_{m0}^{II} = \frac{(r/b)^m - (b/r)^m}{(a/b)^m - (b/a)^m}, \ \ R_{m0}^{*II} = \frac{(a/r)^m - (r/a)^m}{(a/b)^m - (b/a)^m}, \ m \neq 0, \ n = 0 \tag{A3}$$

and for $n = 0$, $m = 0$ it holds:

$$R_{00}^{II} = \frac{\ln(r/b)}{\ln(a/b)}, \ \ R_{00}^{*II} = \frac{\ln(a/r)}{\ln(a/b)}, \ m = 0, \ n = 0 \tag{A4}$$

The functions $R_{mi}^{III}(r)$, $R_{mi}^{*III}(r)$ in Equation (23), are given by:

$$R_{mi}^{III} = \frac{K_m(a_ic)I_m(a_ir) - K_m(a_ir)I_m(a_ic)}{K_m(a_ic)I_m(a_ib) - K_m(a_ib)I_m(a_ic)}, \; i \neq 0 \tag{A5}$$

$$R_{mi}^{*III} = \frac{K_m(a_ir)I_m(a_ib) - K_m(a_ib)I_m(a_ir)}{K_m(a_ic)I_m(a_ib) - K_m(a_ib)I_m(a_ic)}, i \neq 0 \tag{A6}$$

Here a_i are the roots of the transcendental equation: $\omega^2 + a_ig\tan(a_id) = 0$.

Similar to Equations (A1) and (A2), the expressions of the functions $R_{ms}^{IV}(r)$, $R_{ms}^{*IV}(r)$ in Equation (24) are given by:

$$R_{ms}^{IV} = \frac{K_m\left(\frac{s\pi l}{d-h_2}\right)I_m\left(\frac{s\pi r}{d-h_2}\right) - K_m\left(\frac{s\pi r}{d-h_2}\right)I_m\left(\frac{s\pi l}{d-h_2}\right)}{K_m\left(\frac{s\pi l}{d-h_2}\right)I_m\left(\frac{s\pi c}{d-h_2}\right) - K_m\left(\frac{s\pi l}{d-h_2}\right)I_m\left(\frac{s\pi c}{d-h_2}\right)}, \; s \neq 0 \tag{A7}$$

$$R_{ms}^{*IV} = \frac{K_m\left(\frac{s\pi r}{d-h_2}\right)I_m\left(\frac{s\pi c}{d-h_2}\right) - K_m\left(\frac{s\pi c}{d-h_2}\right)I_m\left(\frac{s\pi r}{d-h_2}\right)}{K_m\left(\frac{s\pi l}{d-h_2}\right)I_m\left(\frac{s\pi c}{d-h_2}\right) - K_m\left(\frac{s\pi l}{d-h_2}\right)I_m\left(\frac{s\pi c}{d-h_2}\right)}, \; s \neq 0 \tag{A8}$$

$$R_{m0}^{IV} = \frac{(r/l)^m - (l/r)^m}{(c/l)^m - (l/c)^m}, \;\; R_{m0}^{*IV} = \frac{(c/r)^m - (r/c)^m}{(c/l)^m - (l/c)^m}, \; m \neq 0, \; s = 0 \tag{A9}$$

$$R_{00}^{IV} = \frac{\ln(r/l)}{\ln(c/l)}, \;\; R_{00}^{*IV} = \frac{\ln(c/r)}{\ln(c/l)}, \; m = 0, \; s = 0 \tag{A10}$$

Appendix B

The terms $L_{sq}, L_{si}, L_{ni}, L_{nj}$ defined in Equations (34)–(37) equal to:

$$L_{sq} = \frac{1}{d-h_2}\int_0^{d-h_2} Z_q(z)\cos\left(\frac{s\pi z}{d-h_2}\right)dz = (-1)^s N_q^{-1/2}\frac{a_q(d-h_2)}{a_q^2(d-h_2)^2 - s^2\pi^2}\sin\big(a_q(d-h_2)\big) \text{ for } q \geq 1 \tag{A11}$$

$$L_{si} = \frac{1}{d-h_2}\int\limits_0^{d-h_2} Z_i(z)\cos\left(\frac{s\pi z}{d-h_2}\right)dz$$
$$= (-1)^s N_i^{-1/2}\frac{a_i(d-h_2)}{a_i^2(d-h_2)^2 - s^2\pi^2}\sin(a_i(d-h_2)) \text{ for } i \geq 1 \tag{A12}$$

$$L_{s0} = \frac{1}{d-h_2}\int_0^{d-h_2} Z_0(z)\cos\left(\frac{s\pi z}{d-h_2}\right)dz = (-1)^s N_0^{-1/2}\frac{k(d-h_2)}{k^2(d-h_2)^2 + s^2\pi^2}\sin h(k(d-h_2)) \text{ for } i,q = 0 \tag{A13}$$

$$L_{ni} = \frac{1}{d-h_1}\int_0^{d-h_1} Z_i(z)\cos\left(\frac{n\pi z}{d-h_1}\right)dz = (-1)^n N_i^{-1/2}\frac{a_i(d-h_1)}{a_i^2(d-h_1)^2 - n^2\pi^2}\sin(a_i(d-h_1)) \text{ for } i \geq 1 \tag{A14}$$

$$L_{nj} = \frac{1}{d-h_1}\int_0^{d-h_1} Z_j(z)\cos\left(\frac{n\pi z}{d-h_1}\right)dz = (-1)^n N_j^{-1/2}\frac{a_j(d-h_1)}{a_j^2(d-h_1)^2 - n^2\pi^2}\sin\big(a_j(d-h_1)\big) \text{ for } j \geq 1 \tag{A15}$$

$$L_{n0} = \frac{1}{d-h_1}\int_0^{d-h_1} Z_0(z)\cos\left(\frac{n\pi z}{d-h_1}\right)dz = (-1)^n N_0^{-\frac{1}{2}}\frac{k(d-h_1)}{k^2(d-h_1)^2 + n^2\pi^2}\sin h(k(d-h_1)) \text{ for } j,i = 0 \tag{A16}$$

In Equations (A11)–(A16) the terms N_l, N_0 equal to:

$$N_l = \frac{1}{2}\left[1 + \frac{\sin(2a_ld)}{2a_ld}\right], \;\; N_0 = \frac{1}{2}\left[1 + \frac{\sin h(2kd)}{2kd}\right] \tag{A17}$$

Also, k is related to the wave frequency ω through the dispersion equation and a_l, $l > 0$ are the positive real roots of $\omega^2 + a_lg\tan(a_ld) = 0$.

The terms Λ_j^I, Λ_{mn}^{II}, Λ_{mn}^{*II} in Equation (38) equal to:

$$\Lambda_j^I = a \frac{K_m'(a_j r)\big|_{r=a}}{K_m(a_j a)}, \qquad \Lambda_{mn}^{II} = a \frac{\partial R_{mn}^{II}}{\partial r}\bigg|_{r=a}, \quad \Lambda_{mn}^{*II} = a \frac{\partial R_{mn}^{*II}}{\partial r}\bigg|_{r=a} \tag{A18}$$

Moreover, the terms $D_{mn}^{II}, D_{mn}^{*II}, \Lambda_{mi}^{III}, \Lambda_{mi}^{*III}$ in Equation (39) can be written as:

$$D_{mn}^{II} = b \frac{\partial R_{mn}^{II}}{\partial r}\bigg|_{r=b}, \quad D_{mn}^{*II} = b \frac{\partial R_{mn}^{*II}}{\partial r}\bigg|_{r=b}, \quad \Lambda_{mi}^{III} = b \frac{\partial R_{mi}^{III}}{\partial r}\bigg|_{r=b}, \quad \Lambda_{mi}^{*III} = b \frac{\partial R_{mi}^{*III}}{\partial r}\bigg|_{r=b} \tag{A19}$$

The terms $D_{mi}^{III}, D_{mi}^{*III}, \Lambda_{ms}^{IV}, \Lambda_{ms}^{*IV}$ of Equation (40) equal to:

$$D_{mi}^{III} = c \frac{\partial R_{mi}^{III}}{\partial r}\bigg|_{r=c}, \quad D_{mi}^{*III} = c \frac{\partial R_{mi}^{*III}}{\partial r}\bigg|_{r=c}, \quad \Lambda_{ms}^{IV} = c \frac{\partial R_{ms}^{IV}}{\partial r}\bigg|_{r=c}, \quad \Lambda_{ms}^{*IV} = c \frac{\partial R_{ms}^{*IV}}{\partial r}\bigg|_{r=c} \tag{A20}$$

and the terms Λ_q^V, $D_{ms}^{IV}, D_{ms}^{*IV}$ of Equation (41) can be written as:

$$D_{ms}^{IV} = l \frac{\partial R_{ms}^{IV}}{\partial r}\bigg|_{r=l}, \quad D_{ms}^{*IV} = l \frac{\partial R_{ms}^{*IV}}{\partial r}\bigg|_{r=l}, \quad \Lambda_q^V = l \frac{I_m'(a_q r)\big|_{r=l}}{I_m(a_q l)} \tag{A21}$$

In (A18) and (A21) primes denote derivatives with respect to the radius

Appendix C

The first order horizontal exciting wave forces on the body, based on Equation (42) can be written as:

$$
\begin{aligned}
F_1 = \quad & -\omega^2 \rho \frac{H}{2} a e^{-i\omega t} \sum_{m=0}^{\infty} \varepsilon_m i^m \int_{d-h_1}^{d} \int_0^{2\pi} \Psi_{D,m}^I(r,z) \cos(m\theta)\cos\theta\, d\theta\, dz + \\
& +\omega^2 \rho \frac{H}{2} b e^{-i\omega t} \sum_{m=0}^{\infty} \varepsilon_m i^m \int_{d-h_1}^{d} \int_0^{2\pi} \Psi_{D,m}^{III}(r,z) \cos(m\theta)\cos\theta\, d\theta\, dz - \\
& -\omega^2 \rho \frac{H}{2} c e^{-i\omega t} \sum_{m=0}^{\infty} \varepsilon_m i^m \int_{d-h_2}^{d} \int_0^{2\pi} \Psi_{D,m}^{III}(r,z) \cos(m\theta)\cos\theta\, d\theta\, dz + \\
& +\omega^2 \rho \frac{H}{2} l e^{-i\omega t} \sum_{m=0}^{\infty} \varepsilon_m i^m \int_{d-h_2}^{d} \int_0^{2\pi} \Psi_{D,m}^V(r,z) \cos(m\theta)\cos\theta\, d\theta\, dz = \\
= \quad & -2ikd\left(\pi\rho g a^2 \frac{H}{2}\right)\tan h(kd) \Bigg\{ \frac{N_0^{-\frac{1}{2}}}{(ka)}\left(F_{10}^I - \frac{b}{a}F_{10}^{III}\right)[\sin h(kd) - \sin h(k(d-h_1))] + \\
& + \sum_{j=1}^{J-1} \frac{N_j^{-1/2}}{(\alpha_j a)} F_{1j}^I[\sin(\alpha_j d) - \sin(\alpha_j(d-h_1))] - \frac{b}{a}\sum_{i=1}^{I-1}\frac{N_i^{-1/2}}{(\alpha_i a)}F_{1i}^{III} \\
& [\sin(a_i d) - \sin(a_i(d-h_1))] + \left(\frac{c}{a}\right)^2 \frac{N_0^{-\frac{1}{2}}}{(kc)}\left(F_{10}^{III} - \frac{l}{c}F_{10}^V\right)[\sin h(kd) - \sin h(k(d-h_2))] + \\
& + \left(\frac{c}{a}\right)^2 \sum_{i=1}^{I-1}\frac{N_i^{-1/2}}{(\alpha_i c)}F_{1i}^{III}[\sin(\alpha_i d) - \sin(\alpha_i(d-h_2))] - \left(\frac{c}{a}\right)^2\frac{l}{c}\sum_{q=1}^{Q-1}\frac{N_q^{-1/2}}{(\alpha_q c)}F_{1q}^V[\sin(\alpha_q d) - \sin(\alpha_q(d-h_2))] \Bigg\}
\end{aligned}
\tag{A22}
$$

The first three terms in the parenthesis express the horizontal exciting wave force on the external torus, while the rest three the corresponding force imposed on the internal toroidal cylinder.

Similarly, the vertical exciting wave forces on the body equal to:

$$
\begin{aligned}
F_3 = \ & -\omega^2\rho\tfrac{H}{2}e^{-i\omega t}\sum_{m=0}^{\infty}\varepsilon_m i^m \int_b^a\int_0^{2\pi}\Psi_{D,m}^{II}(r,z)\cos(m\theta)(-1)r\,dr\,d\theta - \\
& -\omega^2\rho\tfrac{H}{2}e^{-i\omega t}\sum_{m=0}^{\infty}\varepsilon_m i^m \int_l^c\int_0^{2\pi}\Psi_{D,m}^{IV}(r,z)\cos(m\theta)(-1)r\,dr\,d\theta = \\
= \ & 2kd\left(\pi\rho g a^2\tfrac{H}{2}\right)\tan h(kd)\left\{\tfrac{1}{2}F_{00}^{II}\left(1-\tfrac{1-(b/a)^2}{2ln(a/b)}\right)-\tfrac{1}{2}F_{00}^{*II}\left(\left(\tfrac{b}{a}\right)^2-\tfrac{1-(b/a)^2}{2ln(a/b)}\right)+\right. \\
& +2\sum_{n=1}^{N-1}(-1)^n\left(\tfrac{d-h_1}{n\pi a}\right)^2\left[F_{0n}^{II}(\Lambda_{0n}^{II}-D_{0n}^{II})+F_{0n}^{*II}(\Lambda_{0n}^{*II}-D_{0n}^{*II})\right]+ \\
& +\tfrac{1}{2}F_{00}^{IV}\left(\tfrac{c}{a}\right)^2\left(1-\tfrac{1-(l/c)^2}{2ln(c/l)}\right)-\tfrac{1}{2}F_{00}^{*IV}\left(\tfrac{c}{a}\right)^2\left(\left(\tfrac{l}{c}\right)^2-\tfrac{1-(l/c)^2}{2ln(c/l)}\right)+ \\
& \left. +2\left(\tfrac{c}{a}\right)^2\sum_{s=1}^{S-1}(-1)^s\left(\tfrac{d-h_2}{s\pi c}\right)^2\left[F_{0s}^{IV}(\Lambda_{0s}^{IV}-D_{0s}^{IV})+F_{0s}^{*II}(\Lambda_{0s}^{*IV}-D_{0s}^{*IV})\right]\right\}
\end{aligned} \tag{A23}
$$

The first three terms in the parenthesis express the vertical exciting wave force on the external torus, while the rest three the corresponding force imposed on the internal toroidal cylinder.

The overturning moment about a horizontal axis lying at an arbitrary distance $z = e$ from the seabed arises from the pressure distribution on the body's vertical walls and on its bottom surface, based on Equation (43), i.e.,

$$
\begin{aligned}
M_1 = \ & -\omega^2\rho\tfrac{H}{2}ae^{-i\omega t}\sum_{m=0}^{\infty}\varepsilon_m i^m \int_{d-h_1}^{d}\int_0^{2\pi}\Psi_{D,m}^{I}(r,z)\cos(m\theta)\cos\theta(z-e)\,d\theta\,dz+ \\
& +\omega^2\rho\tfrac{H}{2}be^{-i\omega t}\sum_{m=0}^{\infty}\varepsilon_m i^m \int_{d-h_1}^{d}\int_0^{2\pi}\Psi_{D,m}^{III}(r,z)\cos(m\theta)\cos\theta(z-e)\,d\theta\,dz- \\
& -\omega^2\rho\tfrac{H}{2}ce^{-i\omega t}\sum_{m=0}^{\infty}\varepsilon_m i^m \int_{d-h_2}^{d}\int_0^{2\pi}\Psi_{D,m}^{III}(r,z)\cos(m\theta)\cos\theta(z-e)\,d\theta\,dz+ \\
& +\omega^2\rho\tfrac{H}{2}le^{-i\omega t}\sum_{m=0}^{\infty}\varepsilon_m i^m \int_{d-h_2}^{d}\int_0^{2\pi}\Psi_{D,m}^{V}(r,z)\cos(m\theta)\cos\theta(z-e)\,d\theta\,dz= \\
& -2ikd\left(\pi\rho g a^3\tfrac{H}{2}\right)\tan h(kd)\Bigg\{\tfrac{N_0^{-\frac{1}{2}}}{(ka)^2}\left(F_{10}^{I}-\tfrac{b}{a}F_{10}^{III}\right)x \\
& [k(d-e)\sin h(kd)-k(d-h_1-e)\sin h(k(d-h_1))-\cos h(kd)+\cos h(k(d-h_1))]+ \\
& +\sum_{j=1}^{J-1}\tfrac{N_j^{-\frac{1}{2}}}{(\alpha_j a)^2}F_{1j}^{I}\left[\alpha_j(d-e)\sin(\alpha_j d)-\alpha_j(d-h_1-e)\sin(\alpha_j(d-h_1))+\right. \\
& \left.+\cos(\alpha_j d)-\cos(\alpha_j(d-h_1))\right]- \\
& -\tfrac{b}{a}\sum_{i=1}^{I-1}\tfrac{N_i^{-\frac{1}{2}}}{(\alpha_i a)^2}F_{1i}^{III}\left[\alpha_i(d-e)\sin(\alpha_i d)-\alpha_i(d-h_1-e)\sin(\alpha_i(d-h_1))+\cos(\alpha_i d)-\right. \\
& \left.-\cos(\alpha_i(d-h_1))\right]+\left(\tfrac{c}{a}\right)^3\tfrac{N_0^{-\frac{1}{2}}}{(kc)^2}\left(F_{10}^{III}-\tfrac{l}{c}F_{10}^{V}\right)x \\
& [k(d-e)\sin h(kd)-k(d-h_2-e)\sin h(k(d-h_2))-\cos h(kd)+\cos h(k(d-h_2))]+ \\
& +\left(\tfrac{c}{a}\right)^3\sum_{i=1}^{I-1}\tfrac{N_i^{-\frac{1}{2}}}{(\alpha_i c)^2}F_{1i}^{III}\left[\alpha_i(d-e)\sin(\alpha_i d)-\alpha_i(d-h_2-e)\sin(\alpha_i(d-h_2))+\cos(\alpha_i d)-\right. \\
& \left.-\cos(\alpha_i(d-h_2))\right]-\left(\tfrac{c}{a}\right)^3\tfrac{l}{c}\sum_{q=1}^{Q-1}\tfrac{N_q^{-\frac{1}{2}}}{(\alpha_q c)^2}F_{1q}^{V}x \\
& \left[\alpha_q(d-e)\sin(\alpha_q d)-\alpha_q(d-h_2-e)\sin(\alpha_q(d-h_2))+\cos(\alpha_q d)-\cos(\alpha_q(d-h_2))\right]\Bigg\}
\end{aligned} \tag{A24}
$$

$$
\begin{aligned}
M_3 = \ & -\omega^2 \rho \tfrac{H}{2} e^{-i\omega t} \sum_{m=0}^{\infty} \varepsilon_m i^m \int_b^a \int_0^{2\pi} \Psi_{D,m}^{II}(r,z) \cos(m\theta)(-1) r^2 dr d\theta - \\
& -\omega^2 \rho \tfrac{H}{2} e^{-i\omega t} \sum_{m=0}^{\infty} \varepsilon_m i^m \int_l^c \int_0^{2\pi} \Psi_{D,m}^{IV}(r,z) \cos(m\theta)(-1) r^2 dr d\theta = \\
= \ & -2ikd \left(\pi \rho g a^3 \tfrac{H}{2} \right) \tan h(kd) \left\{ \tfrac{1}{4} F_{10}^{II}\left(1 - \left(\tfrac{b}{a}\right)^2\right) + \tfrac{1}{4} F_{10}^{*II}\left(\tfrac{b}{a}\right)\left(1 - \left(\tfrac{b}{a}\right)^2\right) + \right. \\
& + 2 \sum_{n=1}^{N-1} (-1)^n \left(\tfrac{d-h_1}{n\pi a}\right)^2 \cdot \left[F_{1n}^{II}\left(\Lambda_{1n}^{II} - \tfrac{b}{a} D_{1n}^{II} - 1\right) + F_{1n}^{*II}\left(\Lambda_{1n}^{*II} + \tfrac{b}{a}(1 - D_{1n}^{*II})\right) \right] + \\
& + \tfrac{1}{4} F_{10}^{IV}\left(\tfrac{c}{a}\right)^3 \left(1 - \left(\tfrac{l}{c}\right)^2\right) + \tfrac{1}{4} F_{10}^{*IV}\left(\tfrac{c}{a}\right)^3 \left(\tfrac{l}{c}\right)\left(1 - \left(\tfrac{l}{c}\right)^2\right) + \\
& + 2 \left(\tfrac{c}{a}\right)^3 \sum_{s=1}^{S-1} (-1)^s \left(\tfrac{d-h_2}{s\pi c}\right)^2 \cdot \left. \left[F_{1s}^{IV}\left(\Lambda_{1s}^{IV} - \tfrac{l}{c} D_{1s}^{IV} - 1\right) + F_{1s}^{*II}\left(\Lambda_{1s}^{*IV} + \tfrac{l}{c}(1 - D_{1s}^{*IV})\right) \right] \right\}
\end{aligned}
\tag{A25}
$$

References

1. Mavrakos, S. Wave loads on a stationary floating bottomless cylindrical body with finite wall thickness. *Appl. Ocean Res.* **1985**, *7*, 213–224. [CrossRef]
2. Molin, B. On the piston and sloshing modes in moonpools. *J. Fluid Mech.* **2001**, *430*, 27–50. [CrossRef]
3. Zheng, S.; Gao, W.; Liu, Y.; Cheng, S. Wave diffraction from a truncated cylinder with a moonpool of arbitrary cross-section: A semi-analytical study. *Ocean Eng.* **2021**, *237*, 109573. [CrossRef]
4. Wu, T.Y.; Yates, G.T. Finite-Amplitude Unsteady Slender-Body Flow Theory. In Proceedings of the 11th Symposium on Naval Hydrodynamics, London, UK, 28 March–2 April 1976.
5. Mavrakos, S. Hydrodynamic characteristics of floating toroidal bodies. *Ocean Eng.* **1997**, *24*, 381–399. [CrossRef]
6. Mavrakos, S.A. Hydrodynamic Characteristics of Two Concentric Surface-Piecing Floating Circular Cylinders. In Proceedings of the 11th International Congress of International Maritime Association of the Mediterranean, IMAM, Lisboa, Portugal, 25–30 September 2005.
7. Garrett, C.J.R. Bottomless harbours. *J. Fluid Mech.* **1970**, *43*, 433–449. [CrossRef]
8. Miloh, T. Wave Loads on a Floating Solar Pond. In Proceedings of the International Workshop on Ship and Platform Motions, Berkeley, CA, USA, 26–28 October 1983; pp. 110–131.
9. Mavrakos, S. Hydrodynamic coefficients for a thick-walled bottomless cylindrical body floating in water of finite depth. *Ocean Eng.* **1988**, *15*, 213–229. [CrossRef]
10. Liu, Y.; Yue, D.K.; Kim, M.-H. First- and second-order responses of a floating toroidal structure in long-crested irregular seas. *Appl. Ocean Res.* **1993**, *15*, 155–167. [CrossRef]
11. Zhou, S.; Mitchell, L. Diffraction of ocean waves around a hollow cylindrical shell structure. *Wave Motion* **2009**, *46*, 78–88. [CrossRef]
12. Zhou, H.; Zhang, H. Radiation and diffraction analysis of a cylindrical body with a moon pool. *J. Hydrodyn.* **2013**, *25*, 196–204. [CrossRef]
13. Chen, X.B.; Liu, H.X.; Duan, W.Y. Semi-analytical solutions to wave diffraction of cylindrical structures with a moonpool with a restricted entrance. *J. Eng. Math.* **2014**, *90*, 51–66. [CrossRef]
14. Liu, H.-X.; Chen, H.-L.; Zhang, L.; Zhang, W.-C.; Liu, M. Quadratic dissipation effect on the moonpool resonance. *China Ocean Eng.* **2017**, *31*, 665–673. [CrossRef]
15. Mavrakos, S.A. Hydrodynamic coefficients in heave of two concentric surface-piercing truncated circular cylinder. *Appl. Ocean. Res.* **2004**, *26*, 84–97. [CrossRef]
16. Mavrakos, S.A.; Chatjigeorgiou, I.K. Second-order hydrodynamic effects on an arrangement of two concentric truncated vertical cylinders. *Mar. Struct.* **2009**, *22*, 545–575. [CrossRef]
17. Mavrakos, S.A.; Chatjigeorgiou, I.K. Second-Order Wave Induced Loads on Vertical Bodies of Revolution. In *Marine Technology and Engineering*; Carlos, G., Soares, Y., Garbatov, N., Fonseca, A.P., Teixeira, Eds.; CRC Press: Boca Raton, FL, USA; Taylor & Francis Group: London, UK, 2011; pp. 479–501. ISBN 978-0-415-69808-5.
18. Cho, I.; Kim, M. Hydrodynamic performance evaluation of a wave energy converter with two concentric vertical cylinders by analytic solutions and model tests. *Ocean Eng.* **2016**, *130*, 498–509. [CrossRef]
19. Kong, F.; Liu, H.; Su, W.; Ao, J.; Chen, H.; Jing, F. Analytical and Numerical Analysis of the Dynamics of a Moonpool Platform–Wave Energy Buoy (MP–WEB). *Energies* **2019**, *12*, 4083. [CrossRef]
20. Abramson, H.N. *The Dynamic Behavior of Liquids in Moving Containers*; NASA SP-106; Scientific and Technical Information Division, National Aeronautics and Space Administration: Washington, DC, USA, 1996.
21. Shipway, B.J.; Evans, D.V. Wave Trapping by Axisymmetric Concentric Cylinders. In Proceedings of the 21st International Conference on Offshore Mechanics and Artic Engineering (OMAE 2002), Oslo, Norway, 23–28 June 2002.
22. McIVER, P.; Newman, J.N. Trapping structures in the three-dimensional water-wave problem. *J. Fluid Mech.* **2003**, *484*, 283–301. [CrossRef]
23. Lu, L.; Teng, B.; Sun, L.; Chen, B. Modelling of multi-bodies in close proximity under water waves—Fluid forces on floating bodies. *Ocean Eng.* **2011**, *38*, 1403–1416. [CrossRef]

24. Lu, L.; Teng, B.; Cheng, L.; Sun, L.; Chen, X. Modelling of multi-bodies in close proximity under water waves—Fluid resonance in narrow gaps. *Sci. China Ser. G Phys. Mech. Astron.* **2010**, *54*, 16–25. [CrossRef]

25. Kristiansen, T.; Faltinsen, O.M. Gap Resonances Analyzed by a Domain-Decomposition Method. In Proceedings of the 26th International Workshop on Water Waves and Floating Bodies, Athens, Greece, 17–20 April 2011.

26. Kristiansen, T.; Faltinsen, O.M. Gap resonances analyzed by a newdomain-decomposition method combining potential and viscous flow. *Appl. Ocean. Res.* **2012**, *34*, 198–208. [CrossRef]

27. Fredriksen, A.G.; Kristiansen, T.; Faltinsen, O.M. Experimental and numerical investigation of wave resonance in moonpools at low forward speed. *Appl. Ocean Res.* **2014**, *47*, 28–46. [CrossRef]

28. Tan, L.; Lu, L.; Tang, G.-Q.; Cheng, L.; Chen, X.-B. A viscous damping model for piston mode resonance. *J. Fluid Mech.* **2019**, *871*, 510–533. [CrossRef]

29. Ntouras, D.; Manolas, D.; Papadakis, G.; Riziotis, V. Exploiting the limit of BEM solvers in moonpool type floaters. *J. Phys. Conf. Ser.* **2020**, *1618*, 082059. [CrossRef]

30. Mavrakos, A.S. Hydrodynamic Parametric Investigation of the Chamber's Geometry on the Efficiency of Floating OSCILLATING Water Column (OWC) Wave Energy Devices. Master' Thesis, School of Naval Architecture and Marine Engineering, National Technical University of Athens, Athens, Greece, July 2019.

31. Wehausen, J.V. The Motion of Floating Bodies. *Annu. Rev. Fluid Mech.* **1971**, *3*, 237–268. [CrossRef]

32. Abramowitz, M.; Stegun, I.A. *Handbook of Mathematical Functions*, 9th ed.; Dover Publications: Mineola, NY, USA, 1970.

33. Ntouras, D.; Papadakis, G. A Coupled Artificial Compressibility Method for Free Surface Flows. *J. Mar. Sci. Eng.* **2020**, *8*, 590. [CrossRef]

34. Hirt, C.W.; Nichols, B.D. Volume of fluid (VOF) method for the dynamics of free boundaries. *J. Comput. Phys.* **1981**, *39*, 201–225. [CrossRef]

35. Chorin, A.J. A Numerical Method for Solving Incompressible Viscous Flow Problems. *J. Comput.-Tional Phys.* **1967**, *2*, 12–26. [CrossRef]

36. Nichols, D. Development of a Free Surface Method Utilizing an Incompressible Multi-Phase Algorithm to Study the Flow about Surface Ships and Underwater Vehicles. Ph.D. Thesis, Department of Aerospace Engineering, Mississippi State University, Starkville, MS, USA, 2002.

37. Kunz, R.F.; Boger, D.A.; Stinebring, D.R.; Chyczewski, T.S.; Lindau, J.W.; Gibeling, H.J.; Venkateswaran, S.; Govindan, T. A preconditioned Navier–Stokes method for two-phase flows with application to cavitation prediction. *Comput. Fluids* **2000**, *29*, 849–875. [CrossRef]

38. Peric, R. Minimizing Undesired Wave Reflection at the Domain Boundaries in Flow Simulations with Forcing Zones. Ph.D. Thesis, Technischen Universität Hamburg, Hamburg, Germany, 2019.

39. Roe, P.L. Approximate Riemann solvers, parameter vectors, and difference schemes. *J. Comput. Phys.* **1981**, *43*, 357–372. [CrossRef]

40. Kelecy, F.; Pletcher, R. The Development of a Free Surface Capturing Approach for Multidimensional Free Surface Flows in Closed Containers. *J. Comput. Phys.* **1997**, *138*, 939–980. [CrossRef]

41. Biedron, R.; Vatsa, V.; Atkins, H. Simulation of Unsteady Flows Using an Unstructured Navier-Stokes Solver on Moving and Stationary Grids. In Proceedings of the 23rd AIAA Applied Aerodynamics Conference, Toronto, ON, USA, 6–9 June 2005; p. 5093.

42. Papadakis, G. Development of a Hybrid Compressible Vortex Particle Method and Application to External Problems including Helicopter Flows. Ph.D. Thesis, Department of Mechanical Engineering, National Technical University of Athens, Athens, Greece, November 2014.

43. Diakakis, K. Computational Analysis of Transitional and Massively Separated Flows with Application to Wind Turbines. Ph.D. Thesis, Department of Mechanical Engineering, National Technical University of Athens, Athens, Greece, 2019.

44. Fredriksen, A.G.; Kristiansen, T.; Faltinsen, O.M. Wave-induced response of a floating two-dimensional body with a moonpool. *Philos. Trans. R. Soc. A Math. Phys. Eng. Sci.* **2015**, *373*, 20140109. [CrossRef]